AIAA JOURNAL
Vol. 49, No. 3, March 2011

# Improving Low-Frequency Characteristics of Recycling/Rescaling Inflow Turbulence Generation

Brandon Morgan,* Johan Larsson,† Soshi Kawai,‡ and Sanjiva K. Lele§
*Stanford University, Stanford, California 94305*

DOI: 10.2514/1.J050705

**For the study of turbulent flows with low-frequency dynamics (e.g. shock-wave/boundary-layer interactions), it is desirable that the inflow turbulence does not contaminate the solution with spurious spatiotemporal correlations introduced by the mechanism of inflow turbulence generation. To investigate the creation and mitigation of these adverse low-frequency effects, large-eddy simulation of a Mach 2.28 boundary layer over an adiabatic flat plate is carried out using a typical recycling/rescaling procedure. Spurious temporal autocorrelations and energy spectral peaks are observed associated with the recycling frequency and its harmonics. Comparisons are made with common "synthetic" turbulence-generation techniques, and improvements to the standard recycling/rescaling procedure are suggested to substantially reduce or eliminate the inherent low-frequency contamination. It is found that by applying a nonconstant reflection or translation operation to the recycled turbulence plane at randomly-distributed time intervals, one is able to maintain realistic turbulence without low-frequency contamination.**

## Nomenclature

| | | |
|---|---|---|
| $C_f$ | = | skin friction coefficient |
| $C_\beta$ | = | dimensionless, user-specified artificial bulk viscosity coefficient |
| $C_\kappa$ | = | dimensionless, user-specified artificial thermal conductivity coefficient |
| $C_\mu$ | = | dimensionless, user-specified artificial dynamic viscosity coefficient |
| $c_s$ | = | speed of sound |
| $E$ | = | total energy |
| $e$ | = | internal energy |
| $f_{\text{sw}}$ | = | switching function |
| $H$ | = | Heaviside function |
| H | = | von Kármán shape factor |
| $L_x, L_y, L_z$ | = | extent of computational mesh |
| $M$ | = | Mach number |
| $N_x, N_y, N_z$ | = | number of grid points in computational mesh |
| $Pr$ | = | Prandtl number |
| $p$ | = | static pressure |
| $R$ | = | gas constant |
| $Re$ | = | Reynolds number |
| $R_{ij}$ | = | component of Reynolds-stress tensor |
| $S$ | = | magnitude of the strain rate tensor |
| $T$ | = | temperature |
| $t$ | = | time |
| $\mathbf{u}$ | = | velocity vector |
| $u_\tau$ | = | friction velocity |
| $\beta$ | = | bulk viscosity |
| $\gamma$ | = | ratio of specific heats |
| $\Delta_{l,\bullet}$ | = | grid spacing in physical space |
| $\Delta\xi_l$ | = | grid spacing in computational space |
| $\delta$ | = | boundary-layer thickness (99% velocity thickness) |
| $\delta_\nu$ | = | viscous length scale |
| $\delta_0$ | = | boundary-layer thickness at inflow boundary |
| $\delta^*$ | = | displacement thickness |
| $\bar{\delta}$ | = | unit tensor |
| $\kappa$ | = | thermal conductivity |
| $\mu$ | = | dynamic viscosity |
| $\nu$ | = | kinematic viscosity |
| $\xi_l$ | = | $l$th generalized coordinate ($l = 1, 2, 3$) |
| $\rho$ | = | density |
| $\tau$ | = | viscous stress tensor |
| $\langle\,\rangle$ | = | mean quantity |

*Subscripts*

| | | |
|---|---|---|
| $f$ | = | fluid contribution to transport term |
| inc | = | incompressible transformation value |
| inl | = | value at inlet |
| $r$ | = | reference quantity |
| rec | = | value at recycling plane |
| VD | = | van Driest transformed quantity |
| $w$ | = | value at wall |
| $\infty$ | = | freestream value |

*Superscripts*

| | | |
|---|---|---|
| inn | = | inner boundary-layer value |
| out | = | outer boundary-layer value |
| * | = | artificial contribution to transport term |
| + | = | wall unit quantity |
| $'$ | = | fluctuating quantity |

Received 3 June 2010; revision received 11 November 2010; accepted for publication 13 November 2010. 

*Graduate Student, Department of Aeronautics and Astronautics, MC 3035. Student Member AIAA.

†Research Associate, Center for Turbulence Research, MC 3035.

‡Postdoctoral Fellow, Center for Turbulence Research, MC 3035. Senior Member AIAA.

§Professor, Department of Aeronautics and Astronautics and Department of Mechanical Engineering, MC 4035. Member AIAA.

## I. Introduction

IN MANY turbulent flows, in particular those involving shock-wave/boundary-layer interactions, a low-frequency unsteadiness develops, which makes accurate prediction with Reynolds-averaged Navier–Stokes solvers questionable [1,2]. To accurately simulate flows of this kind, large-eddy simulation (LES) or direct numerical simulation (DNS) is typically required. Of course, when LES or DNS is used, an accurate prescription of three-dimensional, temporally evolving inflow turbulence is required [3,4]. One option is the simulation of complete laminar-to-turbulent transition. Pirozzoli and Grasso [5], for instance, use a very long domain and force turbulent transition to prescribe the inflow turbulence for their DNS of oblique shock/turbulent boundary-layer interaction (STBLI). This method

has the advantage of being very accurate; however, for situations in which a long time history must be collected (as is often the case when low-frequency dynamics are of interest), such methods are prohibitively expensive. Several methods exist for the more efficient prescription of inflow turbulence, generally falling into one of two categories: synthetic methods and recycling/rescaling (RR) methods. In this paper, examples of both types of inflow condition are compared, and it is suggested how to improve RR methods to eliminate low-frequency contamination associated with the act of recycling.

Synthetic turbulence techniques are characterized by the use of some model to prescribe turbulent fluctuations about a mean flow profile. One of the first synthetic methods is due to Yao and Sandham [6] in their DNS of transonic turbulent flow over a bump; this method was later extended to higher Mach numbers by Li and Coleman (LC) [7]. The LC method attempts to semianalytically prescribe observed features such as near-wall and lifted streaks by enforcing perturbation velocities according to the superposition of several waveform functions. These waveform modes have amplitudes and phase shifts that correspond to desired streak lengths, thicknesses, and periodicity and would be considered fully analytic if not for the addition of high frequency noise to break correlations. Another popular synthetic turbulence method is the digital filtering (DF) approach first developed by Klein et al. [8]. This method, which was later improved by Xie and Castro [9] and Touber and Sandham [3,4], filters a large number of random numbers to prescribe ad hoc first- and second-order statistical moments in velocity perturbation. One might consider the major difference between the DF and LC methods to be that the DF method prescribes a form for the turbulent statistics but not for the turbulent structures, while the LC method prescribes a form of the turbulent structures but not the statistics. These two methods, however, suffer from the drawback that they require a longer "recovery length" than RR over which the computed turbulent flow recovers from modeling errors. Additionally, these methods require some a priori knowledge to prescribe mean velocity, density, and, in the case of DF, Reynolds-stress distributions. Of course, additional synthetic methods exist, such as those of Jarrin et al. [10] and Pamiès et al. [11], which may offer shorter recovery lengths than those of the LC and DF methods. Since the present work is primarily concerned with improvements to RR methods, however, only LC and DF (two of the most commonly used methods in the literature concerning shock-wave/boundary-layer interactions) are selected for comparison.

RR methods are distinguished from synthetic turbulence techniques by the fact that RR techniques do not require any a priori knowledge of mean flow profiles.[¶] Instead, a boundary-layer profile is selected some distance downstream from the inflow boundary, appropriately scaled, and then reintroduced as an updated inflow boundary condition. One of the most popular RR methods, due to Lund et al. [12], was extended to compressible flows by Urbin and Knight [13] for their LES of a Mach 3 turbulent boundary layer. This method decomposes the flowfield variables at the capture plane into a mean and fluctuating component; it then applies the compressible van Driest–Fernholz and Finley transformation so the appropriate incompressible scaling laws can be applied; the scaled profile is then introduced as the inflow boundary condition. Xu and Martin [14] have also proposed an alternative method with rescaling based on Morkovin's hypothesis. Such techniques are often advantageous in that they offer an effective way to control boundary-layer thickness, and they generally recover from modeling errors very quickly. Of course, where low-frequency dynamics are concerned, the major criticism against RR procedures is that, by their nature, RR methods will introduce nonphysical correlations associated with the recycling period. Attempts have been made previously by Spalart et al. [15] and Boles et al. [16] to eliminate this drawback. In the first case, a constant spanwise shift is applied to the recycled profile; however, as we will show, such an approach introduces spatiotemporal cross correlations (essentially transferring the problem without really solving it). In the second case, the method of "random-walk recycling" is introduced. This approach applies a time-varying, continuous shift to the recycled profile to break up correlations, but the effects of such a method on turbulence statistics and physical structure have not yet been widely investigated.

In the present work, several possible improvements to the traditional RR procedure are considered, which take advantage of the homogeneity of turbulence in the spanwise direction. We consider the case of applying a constant spanwise shift (RR + CS) [15], a constant spanwise reflection (RR + CR), dynamic spanwise shifting (RR + DS) similar to random-walk recycling, and a new method dubbed "recycling/rescaling with dynamic reflection" (RR + DR) which applies a nonconstant spanwise reflection to the recycled turbulence profile. To assess the robustness of the RR + DR procedure, we additionally perform a study to determine the effect of altering the frequency of changes in reflection location. While the baseline rescaling procedure used in the present work is that due to Urbin and Knight, dubbed "UKRR," the improvements considered are expected to be relevant to any RR procedure, regardless of the particular scaling laws applied. After a brief discussion of the computational formulation is presented in Secs. II and III, we present in Sec. IV results of simulations using LC, DF, UKRR, RR + CS, RR + CR, RR + DS, and RR + DR.

## II. Mathematical Models

The numerical code used in this study solves the spatially filtered compressible Navier–Stokes equations, which are derived from the compressible Navier–Stokes equations for an ideal nonreactive gas. A sixth-order compact difference scheme [17] is used to solve the governing equations in transformed curvilinear coordinates, and Gauss–Seidel alternate directional implicit factorization [18,19] is used with three Newton–Raphson subiterations for time integration with second-order backwards differencing. Each time step, an eighth-order low-pass spatial filtering scheme [17] (with optimization parameter $\alpha_f = 0.495$) is applied once to the conservative variables to ensure stability, and we use near-boundary formulas developed by Gaitonde and Visbal [20]. To maintain time accuracy of the solution, the time step is selected such that the Courant–Friedrichs–Lewy number is near, but less than, unity. This choice of time-integration scheme and time step size should be sufficiently accurate based on the results of [21].

Since central differencing schemes, such as the compact differencing scheme used in the present study, can generate nonphysical oscillations in regions of high gradient, a shock capturing scheme is desirable; however, such a scheme must not be so dissipative that it eliminates small scales of turbulence. For this reason, the localized artificial diffusivity (LAD) method of shock capturing [21] is applied. The method, which is based on Cook's method [22] of adding artificial coefficients to the fluid transport terms and improved by modification of Mani et al. [23], is enhanced by the addition of a dilatation-based switching function in the formulation of the artificial bulk viscosity. This switching function has the effect of reducing the dissipation for gradients in the near-wall region while localizing dissipation in regions of freestream discontinuity. Aside from the implicit model created by addition of the artificial bulk viscosity and thermal conductivity, no additional subgrid scale (SGS) model is used. We have previously assessed the effect of SGS models [21], and explicit SGS models with low-pass filtering were found to result in additional damping of the resolved turbulence at similar Reynolds number and grid resolution. Detailed description of the governing equations and the LAD scheme can be found in the Appendix and in [21,24–26].

## III. Computational Setup

This study was performed as a part of a larger study on LES of oblique STBLI. As a consequence, an attempt was made to match the experimental flow conditions of Dupont et al. in their investigation of

[¶]While it is true that RR methods often require determination of a mean profile to decompose the recycling plane into a mean and fluctuating component, this profile can be determined on-the-fly, a topic which will be discussed more in Sec. III.

**Table 1 Mesh parameters**

| Mesh | $N_x$ | $N_y$ | $N_z$ | $L_x$ | $L_y$ | $L_z$ | $\Delta x^+$ | $\Delta y^+$ | $\Delta z^+$ | Total points |
|---|---|---|---|---|---|---|---|---|---|---|
| A | 401 | 152 | 81 | $15\delta_r$ | $8.5\delta_r$ | $3\delta_r$ | 15 | 1.0–15 | 15 | 4.92 M |
| B | 801 | 159 | 81 | $30\delta_r$ | $16.0\delta_r$ | $3\delta_r$ | 15 | 1.0–15 | 15 | 10.3 M |

**Table 2 User input required for inflow boundary conditions. An "X" indicates that the information denoted by the column heading is required by the procedure denoted by the row heading**

| Method | $\langle u \rangle$ | $\langle \rho \rangle$ | $\langle T \rangle$ | $\langle u'u' \rangle$ | $\langle v'v' \rangle$ | $\langle w'w' \rangle$ | $\langle u'v' \rangle$ |
|---|---|---|---|---|---|---|---|
| DF | X | X | X | X | X | X | X |
| LC | X | X | X | —— | —— | —— | —— |
| UKRR | —— | —— | —— | —— | —— | —— | —— |
| RR + [x] | —— | —— | —— | —— | —— | —— | —— |

oblique STBLI [27], for which DNS comparison results are readily available [28]. The freestream Mach number, $M_\infty = 2.28$ is taken to match, while the Reynolds number based on momentum thickness ($Re_\theta \approx 1700$) in the present LES simulations is somewhat reduced from both the experiment ($Re_\theta = 5100$) and the DNS ($Re_\theta = 2300$).

Since it is expected that the synthetic turbulence techniques may require a longer length to recover from modeling errors than the RR techniques, we consider two computational meshes: one twice as long as the other in the streamwise direction. The "A" mesh covers $15\delta_r$ in the streamwise direction, $3\delta_r$ in the spanwise direction, and $8.5\delta_r$ in the wall-normal direction ($\delta_r$ in this case refers to the boundary-layer thickness at the downstream capture plane). This mesh is used exclusively for the RR techniques, and the capture plane is selected to be about $12\delta_r$ downstream of the inflow boundary. The "B" mesh covers $30\delta_r$ in the streamwise direction, $3\delta_r$ in the spanwise direction, and $16\delta_r$ in the wall-normal direction. Both meshes stretch from $\Delta y^+ = 1$ at the wall to $\Delta y^+ = 15$ at $y/\delta_r = 1$ and then hold constant wall-normal grid spacing until $y/\delta_r = 3$; above $y/\delta_r = 3$, each grid has 15% stretching until the far boundary. Thus, both grids have the same scaling in the wall-normal direction over $y/\delta_r = 0$ to 3. Table 1 summarizes the grid geometries used; regions of stretching are indicated by a dash. Although we do not perform a mesh refinement study, our previous experience with simulations using the present grid resolution and numerical scheme [26,29] indicates that the present resolution should be sufficient.

In all cases considered, adiabatic nonslip wall conditions are specified at $y/\delta_r = 0$, periodic conditions are specified at $z/\delta_r = 0$ and $z/\delta_r = 3$, and first-order extrapolation is specified at the outflow boundary. The wall-normal extent of each grid is chosen such that a weak shock off the front of the developing boundary layer will exit through the outflow boundary; therefore, freestream conditions are specified at the wall-normal extent boundary. To ensure an "apples-to-apples" comparison of the techniques, time-averaged velocity, density, and Reynolds-stress profiles are captured at the inlet using UKRR, and these profiles are specified as necessary as the mean flow conditions for the synthetic turbulence techniques. The boundary-layer thickness of the captured mean profile is approximately $0.75\delta_r$. We note that in general, such a profile might not be available for use with the synthetic techniques, and as such the present assessment can be considered to represent a best-case scenario for these methods. Table 2 summarizes the user-input required for each of the methods considered. While the RR methods do not require a priori prescription of any mean profile data, these methods still require the determination of a mean profile in order to calculate a fluctuating component at the capture plane. This profile can be determined on-the-fly with RR methods; however, doing so requires a period of time during which the accepted mean profile relaxes to a true turbulent mean. The length of this transient period, of course, will be dependent on the initial conditions and can potentially be quite long. In the present simulation, flow was initialized with a laminar boundary-layer solution with random noise and required about 50 flow-through times (FTTs) before relaxing to a statistically steady state. By comparison, the length of the initial transient for the synthetic methods is only as long as it takes for information to flow through the domain once. In other words, synthetic methods require prescription of some mean quantities while RR methods do not; however, if no mean profile is prescribed, RR methods will require an additional transient period to determine one.

In general, when a mean velocity profile is not available for the synthetic methods, an approximate power law or inverse van Driest transformation is often used, which may require additional approximations about skin friction and/or wall temperature. A temperature–velocity relation is then typically assumed, often invoking the strong Reynolds analogy, along with the assumption that $\partial p/\partial y = 0$, after which the mean density profile can be computed from the ideal gas law.

In the following sections, we describe the three baseline methods (LC, DF, UKRR) and the four potential improvements to RR (constant shifting, constant reflection, dynamic shifting, and dynamic reflection) that are applied in the present work.

### A. Semianalytic Superposition of Waveforms (LC)

The first inflow boundary condition tested is the synthetic technique developed by LC [7] and used by Pirozzoli et al. [30]. This method specifies velocity fluctuations according to Eqs. (1–3). Spanwise disturbances are calculated by enforcing a divergence-free condition $\partial w'/\partial z = -\partial v'/\partial y$:

$$u' = u_\infty \sqrt{\rho_w/\langle\rho\rangle} \sum_{j=1}^{5} a_j U_j \sin(-\omega_j t) \cos(2\pi z/\lambda_{zj} + \phi_j) \qquad (1)$$

$$v' = u_\infty \sqrt{\rho_w/\langle\rho\rangle} \sum_{j=1}^{5} b_j V_j \sin(-\omega_j t) \cos(2\pi z/\lambda_{zj} + \phi_j) \qquad (2)$$

$$U_j = (y/\hat{y}_j)\exp(-y/\hat{y}_j), \qquad V_j = (y/\hat{y}_j)^2 \exp[-(y/\hat{y}_j)^2] \qquad (3)$$

We select constants in Table 3 corresponding to inner-layer disturbances ($j = 1$) propagating at a speed $10u_\tau$ with maximum amplitude at $y^+ = 12$ and outer-layer disturbances that propagate with speed $0.75u_\infty$. These are nearly the same values used in [30] in the simulation of a Mach 2.0 boundary layer with modification to the $b_j$ amplitudes to be more consistent with the original formulation by LC.

To eliminate correlations due to the deterministic specification of Eqs. (1–3), an additional random perturbation with maximum amplitude $0.04u_\infty$ is applied according to Eqs. (4) and (5) for a random variable $r$ selected from a uniform distribution over [0, 1]:

$$f_i' = 0.08u_\infty(r - 0.5)F(y), \qquad i = 1, 2, 3 \qquad (4)$$

**Table 3 Constants for Eqs. (1–3)**

| $j$ | $\hat{y}_j$ | $a_j$ | $b_j$ | $\omega_j$ | $\lambda_{zj}$ | $\phi_j$ |
|---|---|---|---|---|---|---|
| 1 | $12.0\delta_v$ | 1.33 | −0.250 | $0.108u_\tau/\delta_v$ | $128\delta_v$ | 0.0 |
| 2 | $0.298\delta_0$ | 0.33 | −0.007 | $0.839u_\infty/\delta_0$ | $L_z/2$ | 0.1 |
| 3 | $0.447\delta_0$ | 0.33 | −0.007 | $0.419u_\infty/\delta_0$ | $L_z/4$ | 0.2 |
| 4 | $0.596\delta_0$ | 0.33 | −0.007 | $0.210u_\infty/\delta_0$ | $L_z/6$ | 0.3 |
| 5 | $0.447\delta_0$ | 0.33 | −0.007 | $0.336u_\infty/\delta_0$ | $L_z$ | 0.4 |

$$F = \begin{cases} [y/\hat{y}_1]^2 & y < \hat{y}_1 \\ \exp[-((y-\delta_0)/\delta^*_{VD})^2] & y > \delta_0 \\ 1 & \hat{y}_1 \le y \le \delta_0 \end{cases} \quad (5)$$

The inlet velocities are then specified according to Eqs. (6–8). In the present work, no density or temperature fluctuations are specified; although, this could be done by invoking the strong Reynolds analogy:

$$u = \langle u \rangle + u' + f'_1 \quad (6)$$

$$v = v' + f'_2 \quad (7)$$

$$w = w' + f'_3 \quad (8)$$

### B. Digital Filtering

The second inflow boundary condition tested is the DF method of Touber and Sandham [3,4]. This method applies a filter to normally distributed random number fields to correlate perturbation quantities in space and time. These filtered random fields $v^\bullet$ are scaled by prescribed Reynolds-stress values to determine velocities at the inflow boundary according to Eq. (9). While a full description of the filtering operation may be found in [3], Table 4 summarizes the key filter coefficients. It is required that the desired streamwise integral length scale, $I_x$, be specified as well as the two-dimensional filter sizes $N_F$. Since the filter size determines the imposed length scales, two different filter sizes are used for each velocity component: one inside the viscous wall region and one outside. These values were determined from the values used in [3], scaled to the present grid spacing. Again, in the present work, no density or temperature fluctuations are specified; although, this could be done by invoking the strong Reynolds analogy:

$$\begin{bmatrix} u \\ v \\ w \end{bmatrix} = \begin{bmatrix} \langle u \rangle \\ \langle v \rangle \\ \langle w \rangle \end{bmatrix} + \begin{bmatrix} \sqrt{R_{11}} & 0 & 0 \\ R_{21}/\sqrt{R_{11}} & \sqrt{R_{22} - (R_{21}/\sqrt{R_{11}})^2} & 0 \\ 0 & 0 & \sqrt{R_{33}} \end{bmatrix} \begin{bmatrix} v^u \\ v^v \\ v^w \end{bmatrix} \quad (9)$$

### C. Unmodified Recycling/Rescaling (UKRR)

While several RR procedures have been proposed [12–14,31], we consider the method of Urbin and Knight [13]. Figure 1 illustrates the general procedure; a profile is captured some distance downstream from the inflow boundary, scaled appropriately, and reintroduced as an updated inflow condition.

The recycled profile is first decomposed into a mean and fluctuating component, and the mean components are scaled to account for compressibility effects according to Eqs. (10) and (11):

$$\langle u \rangle_{VD} = \frac{\langle u \rangle_\infty}{A} \sin^{-1}\left( A \frac{\langle u \rangle}{\langle u \rangle_\infty} \right), \qquad A = \sqrt{\frac{[(\gamma-1)/2]M^2_\infty Pr_t}{1 + [(\gamma-1)/2]M^2_\infty Pr_t}} \quad (10)$$

**Table 4 Digital filter values**

| Parameter | $u$ | $v$ | $w$ |
|---|---|---|---|
| $I_x$ | $0.7\delta_r$ | $0.28\delta_r$ | $0.28\delta_r$ |
| $N^{inn}_{Fy}$ | 32 | 41 | 27 |
| $N^{out}_{Fy}$ | 60 | 73 | 37 |
| $N_{Fz}$ | 9 | 9 | 18 |

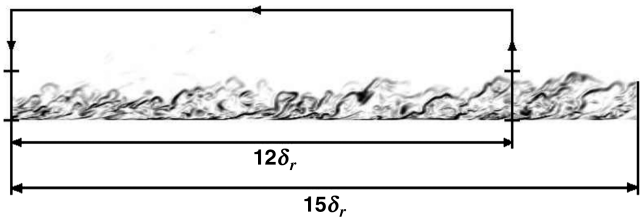


**Fig. 1 Instantaneous density gradient magnitude contours at half span.**

$$\begin{aligned} \langle u \rangle^{inn}_{VD,inl} &= \beta \langle u \rangle_{VD,rec}(y^+_{inl}), \\ \langle u \rangle^{out}_{VD,inl} &= \beta \langle u \rangle_{VD,rec}(y/\delta_{inl}) + (1-\beta)\langle u \rangle_{VD,\infty} \end{aligned} \quad (11)$$

The fluctuating components are next scaled according to Eq. (12):

$$u'^{inn}_{VD,inl} = \beta u'(y^+_{inl}, z, t), \qquad u'^{out}_{VD,inl} = \beta u'(y/\delta_{inl}, z, t) \quad (12)$$

In the preceding equations, the scaling constant $\beta$ is the ratio of friction velocities at the inlet and recycling planes. This ratio is predicted according to the following empirical relationship [32]:

$$\beta = \frac{u_{\tau,inl}}{u_{\tau,rec}} = \left(\frac{\delta_{rec}}{\delta_{inl}}\right)^{1/10} = \left\{ \left[ 1 + \left( \frac{x_{rec} - x_{inl}}{\delta_{inl}} \right) 0.27^{6/5} Re^{-1/5}_{\delta,inl} \right]^{5/6} \right\}^{1/10} \quad (13)$$

Finally, the mean and fluctuating components are combined with a weighted average scheme [12] according to Eqs. (14–17) to determine the new inflow profile (taking $p = p_\infty$ across the boundary layer):

$$u_{inl} = (\langle u \rangle^{inn}_{inl} + u'^{inn}_{inl})[1 - W(y/\delta_{inl})] + (\langle u \rangle^{out}_{inl} + u'^{out}_{inl}) W(y/\delta_{inl}) \quad (14)$$

$$v_{inl} = v'^{inn}_{inl}[1 - W(y/\delta_{inl})] + v'^{out}_{inl} W(y/\delta_{inl}) \quad (15)$$

$$w_{inl} = w'^{inn}_{inl}[1 - W(y/\delta_{inl})] + w'^{out}_{inl} W(y/\delta_{inl}) \quad (16)$$

$$T_{inl} = (\langle T \rangle^{inn}_{inl} + T'^{inn}_{inl})[1 - W(y/\delta_{inl})] + (\langle T \rangle^{out}_{inl} + T'^{out}_{inl}) W(y/\delta_{inl}) \quad (17)$$

where

$$W(\eta) = \frac{1}{2}\left( 1 + \left\{ \tanh\left[ \frac{4(\eta - 0.2)}{0.6\eta + 0.2} \right] \Big/ \tanh(4) \right\} \right) \quad (18)$$

### D. Recycling/Rescaling with Constant Shifting (RR + CS)

The first RR improvement we consider for comparison is the improvement suggested by Spalart et al. [15]. With this improvement, before the rescaled profile is reintroduced as the updated inflow boundary condition, it is first translated a distance of $L_z/2$ (taking advantage of the periodic boundary conditions in the spanwise direction). Since the amount of shifting is held constant in time, this improvement is not expected to do any additional damage to the physical turbulent structures.

### E. Recycling/Rescaling with Constant Reflection (RR + CR)

As an alternative method to RR + CS, we consider applying a constant reflection about the half span location. Since this method maintains the reflection location constant in time, it is also not expected to break apart any physical turbulent structures. However, since the reflection has the effect of moving a structure an amount that

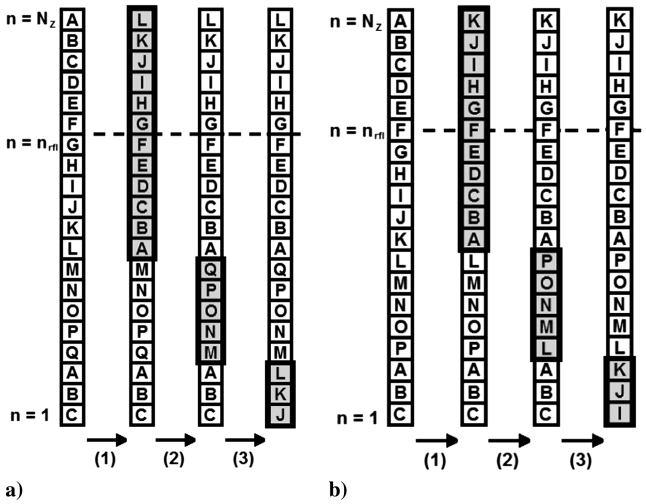


**Fig. 2 An illustration of in-place reflection for a) an even and b) an odd number of points.**

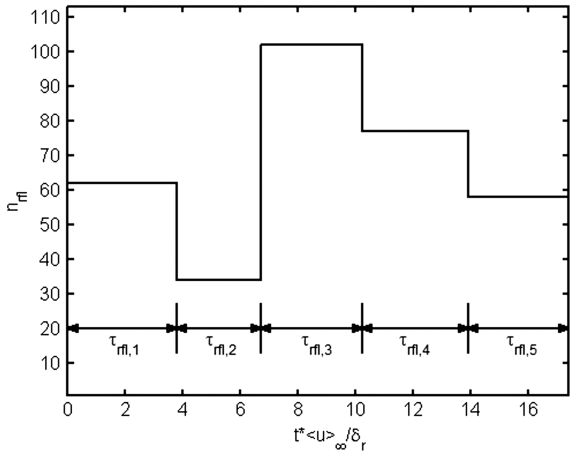


**Fig. 3 Example time history of reflection location.**

is proportional to its distance from the reflection location, it is expected that RR + CR should provide a generally higher degree of "scrambling" the turbulent structures in the spanwise direction than RR + CS.

When implemented properly, the reflection operation can be accomplished with no additional memory allocation and requires only a single pass over the recycled profile data. Figures 2a and 2b illustrate how reflection about an arbitrary point $n_{\text{rfl}}$ is accomplished for grids with $N_z$ even and odd, respectively. In these figures, an example is considered in which a spanwise vector of conservative flow variables at the inlet and arbitrary wall-normal station are to be reflected. A three-point periodic overlap is assumed, and the set of conservative flow variables at a grid point is illustrated as a letter. When a "swap" operation is performed between two spanwise locations, the values of the conservative flow variables in the two locations are exchanged, and the sign of the spanwise velocity in each is flipped to preserve streamwise vorticity. The procedure for reflecting the vectors is then accomplished in three steps: first, all of the values between $n = n_{\text{rfl}}$ and the nearest boundary are swapped with their corresponding location on the opposite side of the reflection boundary; next, points in the remaining unswapped section (excluding the second boundary) are swapped about the center of the unswapped section; finally, the remaining boundary is filled in with values from the first boundary. The difference between swapping an even and odd number of points is simply the interpretation of $n_{\text{rfl}}$. When $N_z$ is odd, $n_{\text{rfl}}$ indicates a stationary point about which the reflection occurs, and when $N_z$ is even, $n_{\text{rfl}}$ indicates an intergridpoint boundary about which reflection occurs. Additionally, when the number of periodic overlap points is odd, the number of unswapped points in the second step will always be odd, and when the number of overlap points is even, the number of unswapped points in the second step will always be even.

As with RR + CS, however, if the recycling length is not long enough to completely decorrelate structures in time, the capture location will "see" the same structure again after it has been shifted twice. For this reason, it may be necessary to apply an additional level of scrambling.

### F. Recycling/Rescaling with Dynamic Reflection (RR + DR)

As with RR + CR, when using RR with dynamic reflection (RR + DR), before the scaled profile is reintroduced as updated inflow conditions, it is reflected about a spanwise station. To provide additional scrambling, however, the spanwise station about which the reflection occurs is selected according to a uniformly distributed random number $n_{\text{rfl}} \in (1, N_z)$, which is updated occasionally according to a second random variable, $\lambda_{\text{rfl}}$. This second random variable, $\lambda_{\text{rfl}}$, represents a characteristic streamwise streak length and is selected from a normal distribution; it is then converted to a nondimensional time scale based on the convective velocity of a streak in the outer boundary layer according to Eq. (19):

$$\tau_{\text{rfl}} = \frac{\lambda_{\text{rfl}}}{\delta_r(0.8M_\infty)} \tag{19}$$

At the beginning of the simulation, a value is selected for $n_{\text{rfl}}$, and a value is selected for $\lambda_{\text{rfl}}$. After an amount of time equal to $\tau_{\text{rfl}}$ has passed, new values of both $n_{\text{rfl}}$ and $\lambda_{\text{rfl}}$ are selected, and the process is repeated. Figure 3 illustrates a typical time history. Of course, altering the reflection location discontinuously will create momentary discontinuities in turbulent structures at the inlet. In Sec. IV, we assess the effect of these periodic discontinuities on the turbulence statistics and acoustics. We also explore the effect of varying the distributions from which the random variable $\lambda_{\text{rfl}}$ is selected.

### G. Recycling/Rescaling with Dynamic Shifting (RR + DS)

With RR with dynamic shifting (RR + DS), a nonconstant spanwise shift is applied to the rescaled profile before it is reintroduced as updated inflow boundary conditions. Unlike random-walk recycling [16], which uses a continuous shift (updating the amount of shift every time step), RR + DS updates the amount of shifting, $n_{\text{shift}}$, discontinuously in the same manner that the reflection location $n_{\text{rfl}}$ is updated for RR + DR (as described in the previous section). We consider RR + DS as a comparison to RR + DR in order to determine whether dynamic reflection or translation might provide some heretofore unpredicted benefit over the other.

## IV. Results

In this section, we discuss the simulation of a turbulent boundary layer developing over an adiabatic flat plate using the numerical methods presented in Sec. II and the several different methods for specifying inflow conditions presented in Sec. III. Unless otherwise noted, time-averaged statistics are also spanwise averaged, and statistics reported at a single streamwise location are reported at the reference location $x_r$ where $\delta(x) = \delta_r$. Data are collected after simulations have reached a statistically steady state, and averages are taken over a period of 342 $\delta_r/u_\infty$ (about 30 FTTs on mesh A). Methods are to be compared based on their relative ability to realistically predict turbulent statistics and to recover from modeling errors. We will approach these comparisons in three sections: first, baseline RR is compared with synthetic methods; next, reflection and shifting improvements to standard RR are compared; and finally, a parametric variation is performed on the random variables that determine how often the reflection location is changed using RR + DR.

**Table 5 Group 1 characteristic properties at reference location**

| Method | $x_r/\delta_r$ | $Re_\delta$ | $Re_{\delta*}$ | $Re_\theta$ | $H(\delta^*/\theta)$ | $C_f$ | $u_\tau/u_\infty$ |
|---|---|---|---|---|---|---|---|
| UKRR | 12.7 | 18,900 | 5340 | 1660 | 3.22 | $2.84 \times 10^{-3}$ | 0.0505 |
| DF | 13.8 | 18,900 | 5500 | 1690 | 3.26 | $2.78 \times 10^{-3}$ | 0.0502 |
| LC | 22.7 | 18,800 | 6050 | 1710 | 3.54 | $2.79 \times 10^{-3}$ | 0.0508 |
| DNS [28] | 25.2 | 29,000 | 8320 | 2330 | 3.60 | $2.51 \times 10^{-3}$ | 0.0493 |

### A. Group 1: UKRR, DF, and LC

Our first goal is to establish a baseline comparison. We do this by first comparing standard RR with the synthetic techniques. Solution quality is established when possible by comparing to DNS computation by Pirozzoli and Bernardini [28], which was generated using a RR method similar to Xu and Martin [14] with a constant spanwise shift of $L_z/2$ (as in RR + CS). Table 5 summarizes flow properties at the reference station for each method. Recall that the reference location, $x_r$, is the location at which $\delta(x) = \delta_r$ and at which turbulence profiles are to be compared. Since all three methods are prescribed the same mean profile at the inlet, the distance $x_r$ may also be thought of as one measure of a method's ability to recover from modeling errors.

In Figs. 4a and 4b we compare the first-order turbulence statistics at the reference location for the three methods under consideration with DNS [28] and experiment [33]. It is clear in Fig. 4a that the van Driest transformed velocity profiles of all methods collapse quite nicely to the DNS solution. In Fig. 4b, however, we see that, while the UKRR and DF turbulence intensity profiles generally agree with DNS and with experiment, the LC solution differs greatly: an indication that the LC boundary layer has not become fully developed by the reference location. In fact, profiles at stations further downstream confirm that the LC boundary layer does not become fully developed in the computational domain used.

Another popular indicator of whether a boundary layer has reached equilibrium is skin friction coefficient. The van Driest 2 transformation [34], given by Eq. (20), is used to compare with incompressible skin friction correlations by von Karman and Blasius (given in [35]). Equation (21) [36] is used to transform compressible momentum thickness into an equivalent incompressible momentum thickness for comparison:

$$C_{f\text{inc}} = \frac{\langle T\rangle_w/T_\infty - 1}{\arcsin^2\alpha} C_f, \qquad \alpha = \frac{\langle T\rangle_w/T_\infty - 1}{\sqrt{\langle T\rangle_w/T_\infty(\langle T\rangle_w/T_\infty - 1)}} \tag{20}$$

$$Re_{\theta\text{inc}} = \frac{\mu_\infty}{\langle\mu\rangle_w} Re_\theta \tag{21}$$

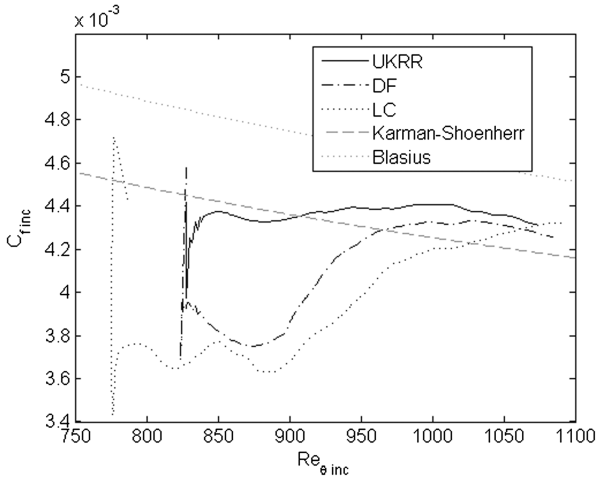


**Fig. 5 Comparison of skin friction evolution among group 1 inflow conditions.**

Figure 5 compares the computed skin friction values for each of the three inflow conditions currently under consideration. One may consider the distance between the two empirical curves as a rough estimate of error in skin friction measurements; so large dips away from these curves indicate regions of large error due to modeling errors. If we were to judge equilibrium based on skin friction lying between the two empirical curves, then it appears as if UKRR meets this criterion around $Re_{\theta\text{inc}} = 910 (x/\delta_r = 3.0)$; DF meets this criterion around $Re_{\theta\text{inc}} = 965 (x/\delta_r = 7.1)$; and LC meets this criterion around $Re_{\theta\text{inc}} = 1030 (x/\delta_r = 19.1)$. However, a better estimate would likely be the point at which a $C_f$ curve lies between the two empirical relations and begins a decreasing trend at an inflection point. Using this criterion, we would say that UKRR reaches equilibrium around $Re_{\theta\text{inc}} = 1010 (x/\delta_r = 9.1)$, DF reaches equilibrium around $Re_{\theta\text{inc}} = 1035 (x/\delta_r = 10.6)$, and LC does not reach equilibrium in the domain. This assessment agrees with the conclusions drawn from Fig. 4b.

Yet another way to determine the inflow recovery length is to consider the evolution of Reynolds-stress quantities. Figure 6 shows contours of Reynolds-stress components for each of the group 1 inflow conditions against a wall-normal coordinate that is scaled by the local boundary-layer thickness. We expect that when a boundary layer has reached equilibrium, these contours should be nearly horizontal in the outer boundary layer. As we have observed before, the LC results do not appear to reach equilibrium in the domain. Figure 6a provides the reason; we notice in this figure that the LC contours indicate a much higher degree of streamwise turbulence

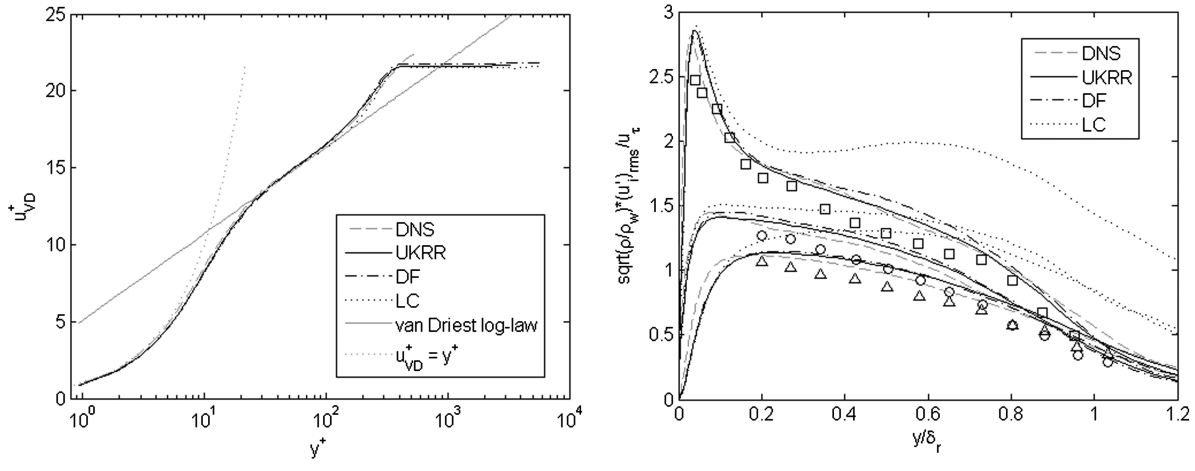


a) b)

**Fig. 4 Comparison of a) van Driest transformed mean streamwise velocity profiles (log law given by $u^+_{\text{VD}} = 5.1 + 1/0.41 * \log[y+]$) and b) density-scaled RMS turbulence intensity. Symbols taken from experiment by Erm and Jourbert [33] (□: streamwise, ○: spanwise, Δ: wall-normal).**

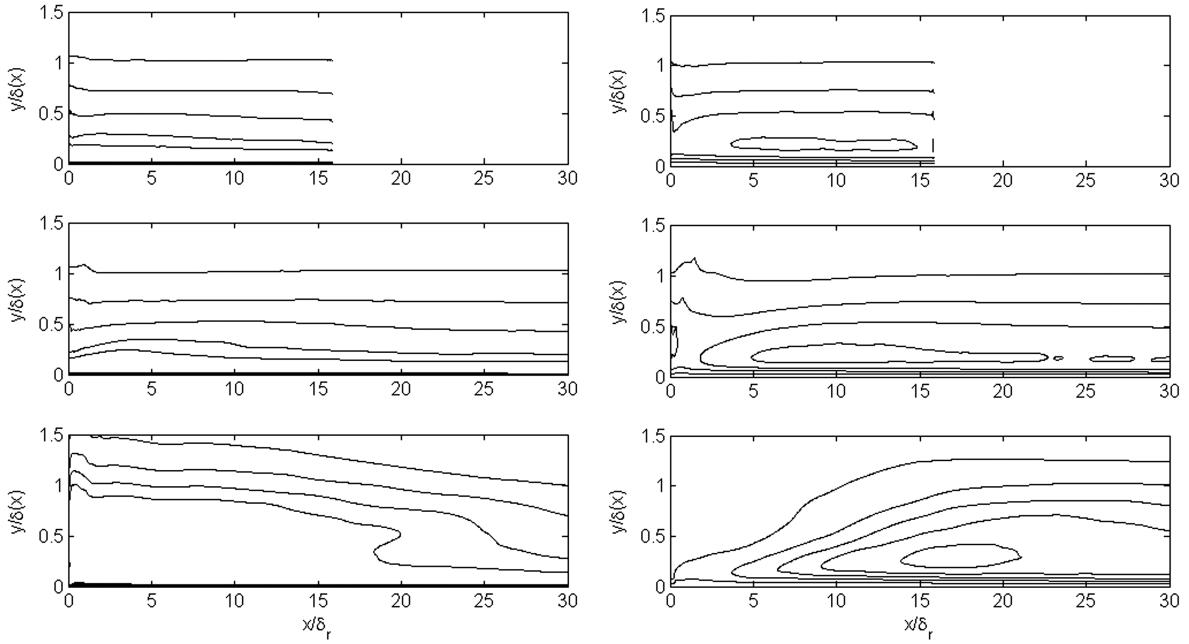


**Fig. 6 Reynolds-stress distribution: five equally spaced contours of a) $\langle u'u' \rangle / u_\tau^2$ between 0.1 and 3.0 and b) $\langle v'v' \rangle / u_\tau^2$ between 0.1 and 1.2. From top to bottom in each figure: UKRR, DF, LC.**

intensity near the inflow boundary than the other two methods. Indeed, the magnitude of the streamwise fluctuations specified by the LC boundary conditions is much higher in comparison to the other methods: on the order of about $0.15u_\infty$ with LC versus $0.05u_\infty$ with the other methods. This is not unexpected based on the formulation, however. Recall Eqs. (1), (4), and (6). High frequency fluctuations are specified with a maximum of 4% of $u_\infty$. In order that the fluctuating streamwise velocity be resolvable, $u'$ must be much larger than the high frequency noise. Unfortunately, the high magnitude of the fluctuating quantities appears to be responsible for the creation of a considerable compression wave, which essentially changes the mean profile at the inlet that is seen by the rest of the flow. (This is also the reason why the LC initial skin friction in Fig. 4 does not agree with the other methods.) By visual estimation, for UKRR and DF, it appears as if the two outermost horizontal contours in all statistics become completely horizontal by $x/\delta_r$ approximately equal to 11 and 15, respectively. It is interesting to note that, while only a qualitative assessment, these recovery lengths are longer than those determined earlier from the skin friction. One might infer that, since the skin friction is apparently recovered faster than second-order statistical moments, the closer a method is able to predict these moments at the inlet, the shorter the recovery length will need to be.

The results of the previous section are not unexpected. We have established confidence in our baseline RR and observed that with UKRR, an equilibrium boundary layer may be obtained over a shorter computational domain than with DF or LC. This motivates the following sections, which investigate ways to improve the standard RR procedure to eliminate nonphysical temporal autocorrelations.

### B. Group 2: UKRR, RR + CS, RR + DS, RR + CR, and RR + DR

In this section, we investigate how the addition of spanwise scrambling affects the solution with respect to our baseline RR simulation. We consider both constant and dynamic spanwise translation and reflection. The parameter that controls how often dynamic shifting occurs ($\lambda_{\text{rfl}}$ in Sec. III.F) in both RR + DS and RR + DR is selected in this section from a normal distribution with a mean of $5\delta_r$ and a standard deviation of $1\delta_r$. In Sec. IV.C, we

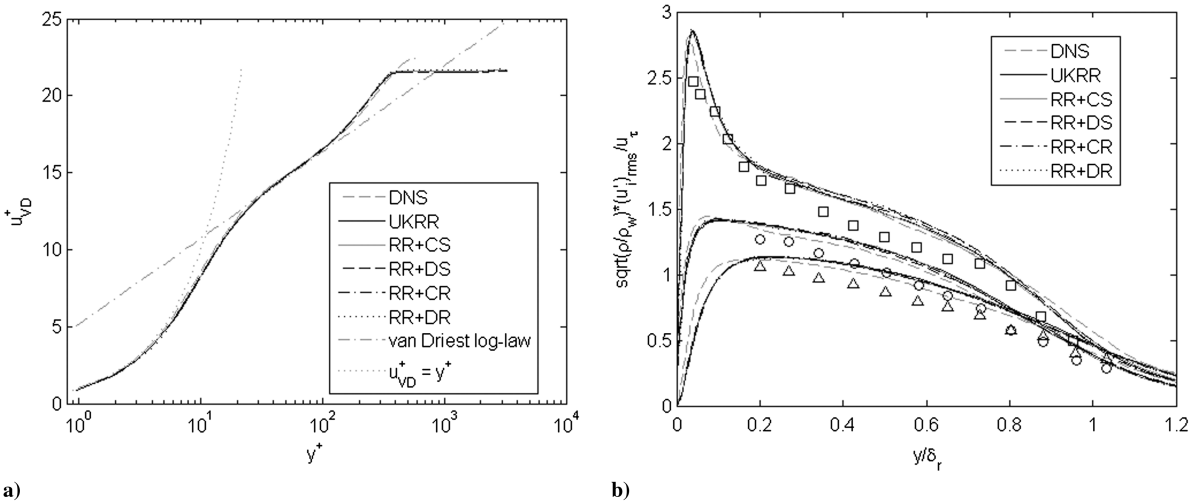


**Fig. 7 Comparison of a) van Driest transformed mean streamwise velocity profiles (log law given by $u_{\text{VD}}^+ = 5.1 + 1/0.41 * \log[y+]$) and b) density-scaled RMS turbulence intensity. Symbols taken from experiment by Erm and Jourbert [33] (□: streamwise, ○: spanwise, Δ: wall-normal).**

**Table 6 Group 2 characteristic properties at reference location**

| Method | $x_r/\delta_r$ | $Re_\delta$ | $Re_{\delta*}$ | $Re_\theta$ | H $(\delta^*/\theta)$ | $C_f$ | $u_\tau/u_\infty$ |
|---|---|---|---|---|---|---|---|
| UKRR | 12.7 | 18,900 | 5340 | 1660 | 3.22 | $2.84 \times 10^{-3}$ | 0.0505 |
| RR + CS | 12.6 | 19,000 | 5340 | 1660 | 3.22 | $2.84 \times 10^{-3}$ | 0.0505 |
| RR + DS | 12.6 | 19,100 | 5350 | 1660 | 3.22 | $2.85 \times 10^{-3}$ | 0.0507 |
| RR + CR | 12.6 | 19,000 | 5340 | 1660 | 3.22 | $2.85 \times 10^{-3}$ | 0.0507 |
| RR + DR | 12.8 | 18,800 | 5330 | 1650 | 3.23 | $2.83 \times 10^{-3}$ | 0.0505 |
| DNS [28] | 25.2 | 29,000 | 8320 | 2330 | 3.60 | $2.51 \times 10^{-3}$ | 0.0493 |

investigate the effect of altering these parameters. Table 6 summarizes flow properties at the reference station for each method considered in group 2. We observe that there is no significant variation in these properties among the various improved methods.

Figures 7a and 7b compare the van Driest transformed streamwise velocity profile and root-mean-square (RMS) velocity fluctuations, respectively, among the methods in Table 6. In Fig. 7a, we again see that all methods collapse to the DNS profile and agree, as expected, with theory in the viscous sublayer and log layer. In Fig. 7b, we see that the present work achieves generally good agreement with DNS; differences that are observed are likely the result of differences in numerical scheme, Reynolds number, and grid resolution. The more important observation, however, is that we see virtually no difference in turbulence intensity among the improved methods, which implies that any damage done to the turbulence structure in the dynamic methods must be recovered quickly. This premise will be investigated in more detail in Sec. IV.C by looking at RMS vorticity, intermittency, and spanwise energy spectra.

Figure 8 additionally shows the skin friction evolution of the four improved methods under consideration. We see that they all generally follow the same evolution, with RR + DR taking slightly longer to fall between the empirical relations; however, all methods appear to reach inflection within the empirical curves after nearly the same development length. This observation further supports the idea that modeling errors due to dynamic shifting and reflection are recovered very quickly.

Having established that the first-order statistics and development length are generally unaffected by the addition of the proposed methods, we next seek to quantify the effect each method has on the spatiotemporal correlations that we wish to eliminate. Figures 9a and 9b illustrate contours of streamwise UKRR velocity correlation as a function of space and time. In Fig. 9a, the spatial dimension under consideration is the streamwise direction, $x$, and correlations are measured from the reference location $x = x_r$ at a height $y/\delta_r = 0.7$ in the outer boundary layer, where the most significant correlations are observed. We observe in this figure three parallel streaks that weaken in intensity as one sweeps from left-to-right across the figure. Sweeping from left to right in this fashion, the first streak represents correlation due to streaks convecting from the inlet to the reference location; this streak is physical (notice that it extends between zero on the ordinate axis and one FTT on the abscissa). The next two streaks indicate that even after recycling through twice (and perhaps further if the plot were extended in time), large structures in the outer boundary layer fail to become decorrelated with standard RR. Figure 9b tells a similar story; here, the spatial dimension under consideration is the spanwise direction. Again, sweeping from left to right in this image, the first correlation is physical and represents the spanwise integral length scale, but the next two are spurious. Recalling that the reference location is located a distance $12.7\delta_r$ downstream of the inlet, based on these plots which show spurious correlations remaining in time out through about 2.25 FTTs, one might estimate that without some kind of improvement, UKRR would require around $38.1\delta_r$ streamwise domain to decorrelate, which would seriously undermine one of the chief advantages of RR methods—that of relatively short recovery distances.

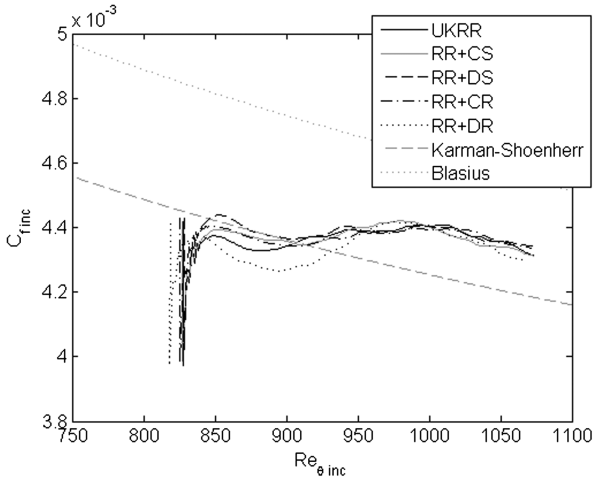


**Fig. 8 Comparison of skin friction evolution among group 2 inflow conditions.**

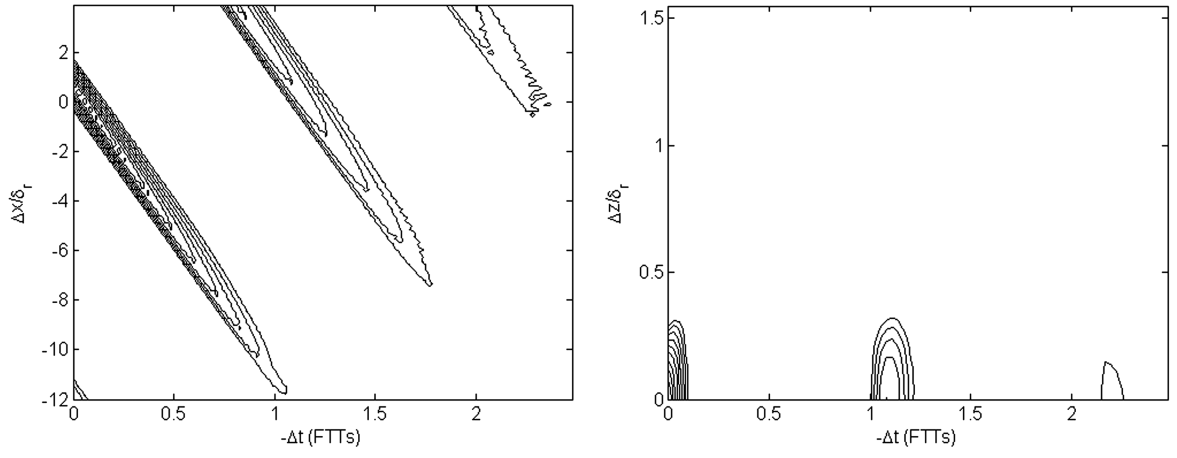


a) b)

**Fig. 9 Ten logarithmically spaced contours of UKRR streamwise velocity spatiotemporal cross correlation function between 0.1 and 1.0 at $y/\delta_r = 0.7$: a) streamwise direction and time, $C_{u'(xr,y,z,t)u'(xr+\Delta x,y,z,t+\Delta t)}$, and b) spanwise direction and time, $C_{u'(xr,y,z,t)u'(xr,y,z+\Delta z,t+\Delta t)}$.**

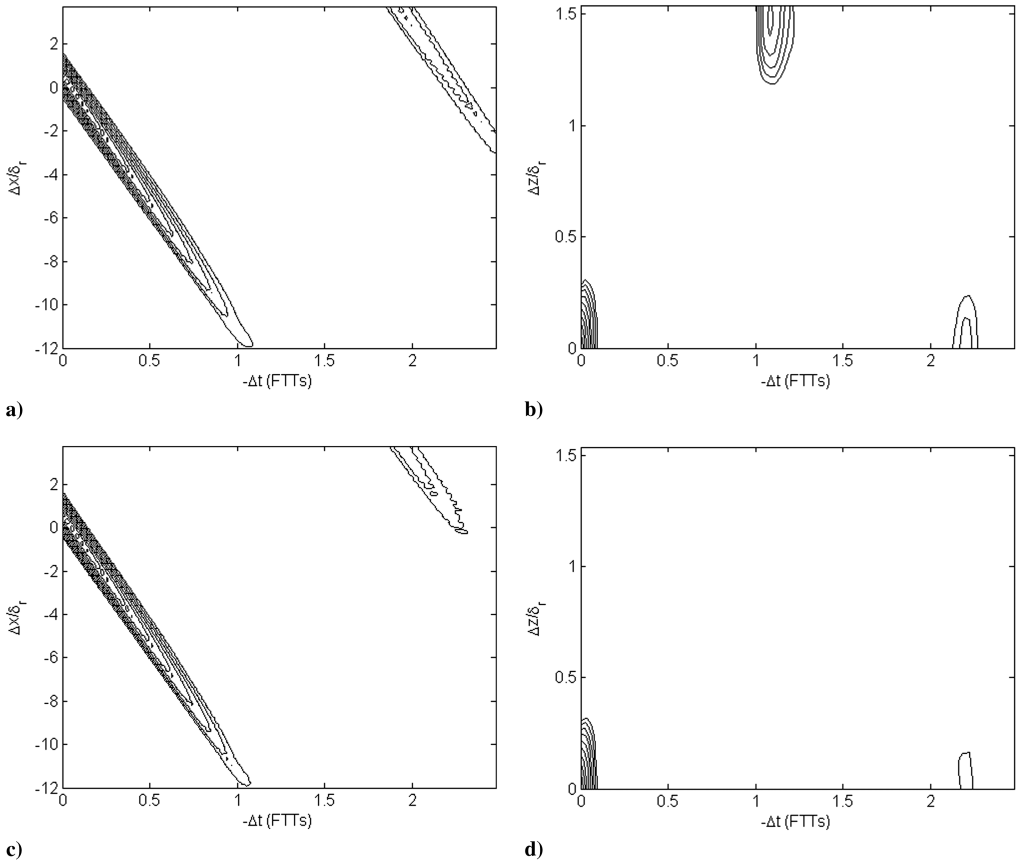


**Fig. 10 Ten logarithmically spaced contours of streamwise velocity spatiotemporal cross correlation function between 0.1 and 1.0 at $y/\delta_r = 0.7$: a) RR + CS streamwise direction and time, $C_{u'(xr,y,z,t)u'(xr+\Delta x,y,z,t+\Delta t)}$, b) RR + CS spanwise direction and time, $C_{u'(xr,y,z,t)u'(xr,y,z+\Delta z,t+\Delta t)}$, c) RR + CR streamwise direction and time, $C_{u'(xr,y,z,t)u'(xr+\Delta x,y,z,t+\Delta t)}$, and d) RR + CR spanwise direction and time, $C_{u'(xr,y,z,t)u'(xr,y,z+\Delta z,t+\Delta t)}$.**

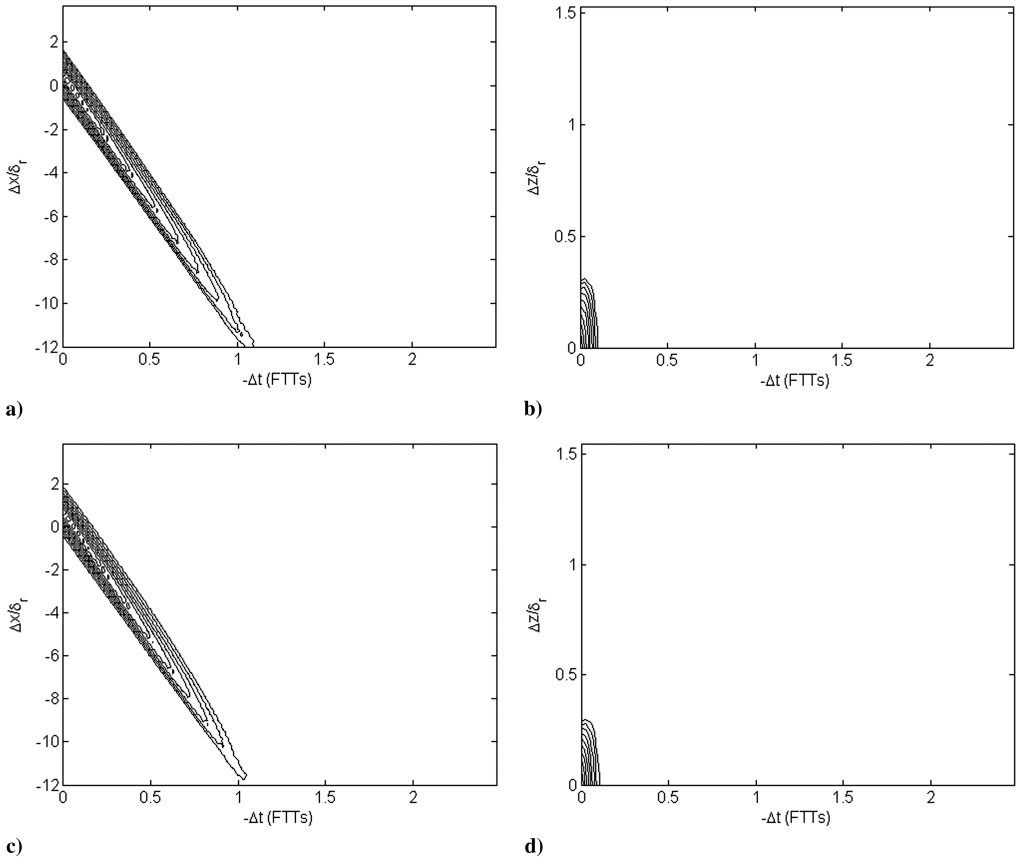


**Fig. 11 Ten logarithmically spaced contours of streamwise velocity spatiotemporal cross correlation function between 0.1 and 1.0 at $y/\delta_r = 0.7$: a) RR + DS streamwise direction and time, $C_{u'(xr,y,z,t)u'(xr+\Delta x,y,z,t+\Delta t)}$, b) RR + DS spanwise direction and time, $C_{u'(xr,y,z,t)u'(xr,y,z+\Delta z,t+\Delta t)}$, c) RR + DR streamwise direction and time, $C_{u'(xr,y,z,t)u'(xr+\Delta x,y,z,t+\Delta t)}$, and d) RR + DR spanwise direction and time, $C_{u'(xr,y,z,t)u'(xr,y,z+\Delta z,t+\Delta t)}$.**

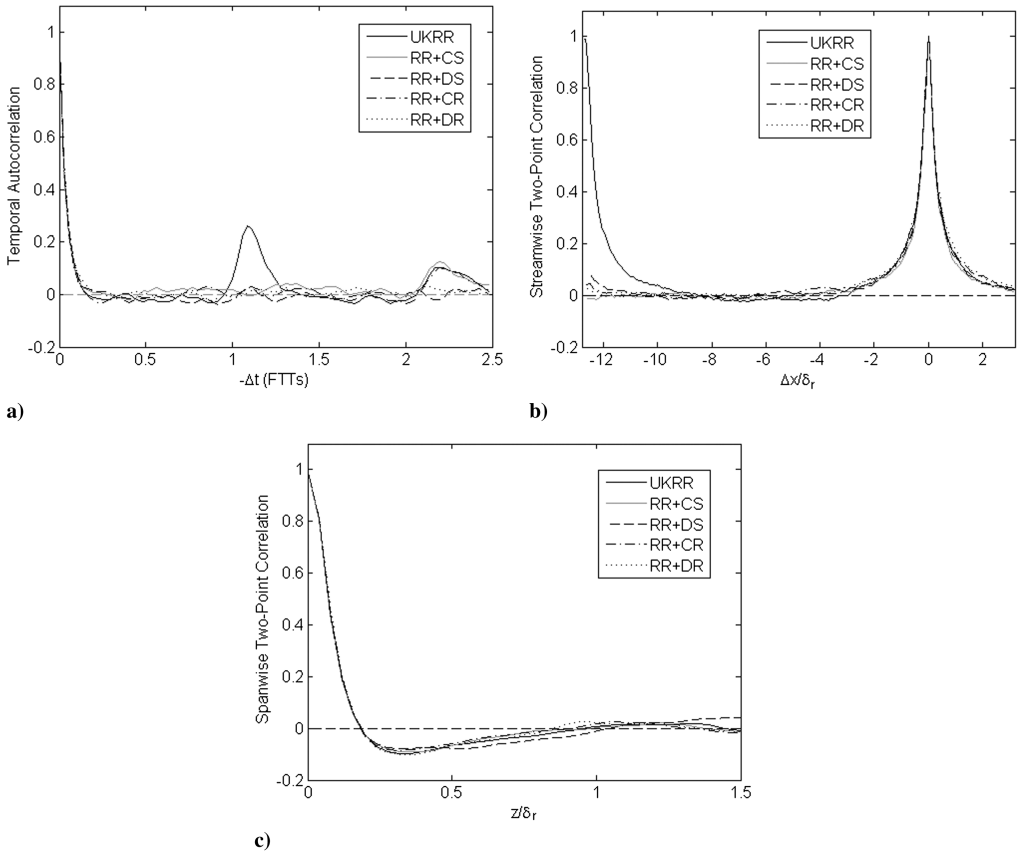


**Fig. 12 Comparison of streamwise velocity two-point correlations and autocorrelations: a) temporal autocorrelation function at $x/\delta_r = x_r$ and $y/\delta_r = 0.7$, b) streamwise two-point correlation function at $x/\delta_r = x_r$ and $y/\delta_r = 0.1$, and c) spanwise two-point correlation function at $x/\delta_r = x_r$ and $y/\delta_r = 0.1$.**

In Figs. 10a–10d, we plot the correlation maps associated with the methods that apply constant spanwise scrambling by means of translation (Figs. 10a and 10b) or reflection (Figs. 10c and 10d). Comparing Fig. 10a with Fig. 9a, we see that while RR + CS appears to eliminate the first spurious streak, the second still remains. Furthermore, by observing Fig. 10b, we see that the temporal autocorrelation at one FTT is essentially replaced with two-point cross correlation that was not previously present. In essence, this method has "hidden" the first correlation without really eliminating it and still fails to eliminate the second spurious correlation at two FTTs. With RR + CR, since profiles are essentially translated a distance that is proportional with their distance from the reflection

**Table 7 Summary of parametric variation on RR + DR**

| Method | Mean $(\lambda_{\text{rfl}})/\delta_r$ | Standard deviation $(\lambda_{\text{rfl}})/\delta_r$ |
|---|---|---|
| RR + DR (A) | 5.00 | 1.00 |
| RR + DR (B) | 2.50 | 0.50 |
| RR + DR (C) | 10.0 | 2.00 |
| RR + DR (D) | 2.50 | 1.00 |

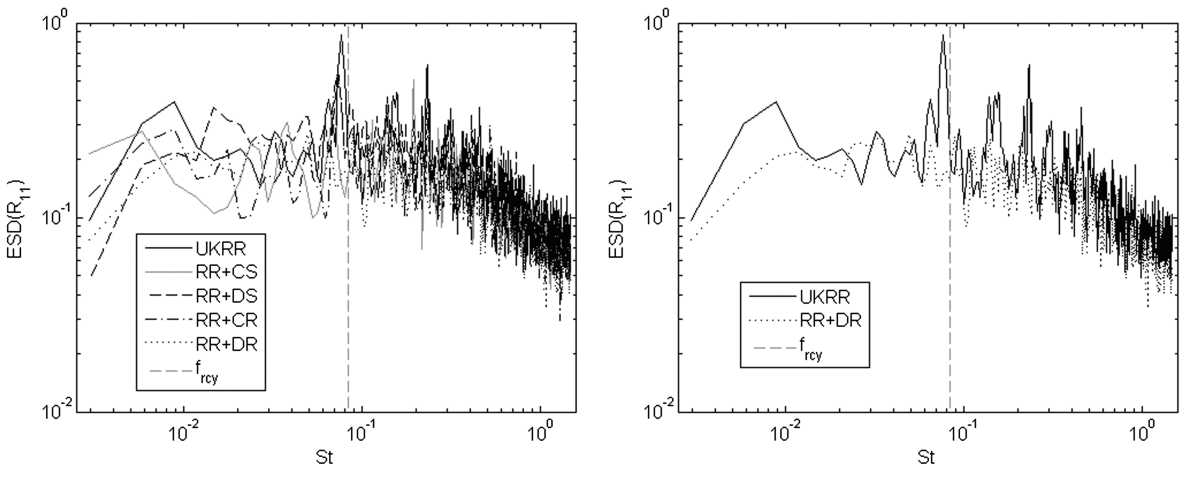


**Fig. 13 Energy spectral density of $R_{11}$ time signal at $x/\delta_r = x_r$ and $y/\delta_r = 0.7$: a) comparison of group 2 methods and b) focused comparison of energetic peak at recycling frequency.**

**Table 8 Group 3 characteristic properties at reference location**

| Method | $x_r/\delta_r$ | $Re_\delta$ | $Re_{\delta*}$ | $Re_\theta$ | H ($\delta^*/\theta$) | $C_f$ | $u_\tau/u_\infty$ |
|---|---|---|---|---|---|---|---|
| UKRR | 12.7 | 18,900 | 5340 | 1660 | 3.22 | $2.84 \times 10^{-3}$ | 0.0505 |
| RR + DR (A) | 12.8 | 18,800 | 5330 | 1650 | 3.23 | $2.83 \times 10^{-3}$ | 0.0505 |
| RR + DR (B) | 12.6 | 19,000 | 5330 | 1650 | 3.23 | $2.83 \times 10^{-3}$ | 0.0505 |
| RR + DR (C) | 12.6 | 18,700 | 5320 | 1640 | 3.24 | $2.83 \times 10^{-3}$ | 0.0505 |
| RR + DR (D) | 13.1 | 18,400 | 5310 | 1640 | 3.25 | $2.82 \times 10^{-3}$ | 0.0504 |
| DNS [28] | 25.2 | 29,000 | 8320 | 2330 | 3.60 | $2.51 \times 10^{-3}$ | 0.0493 |

location (rather than a constant distance, as with RR + CS), we see in Figs. 10c and 10d that a reflection operation does appear to eliminate the first spurious correlation; however, it fails to eliminate the second spurious streak. Based on this comparison, if one were to select a method of constant spanwise scrambling, reflection would appear to be the superior choice; however, neither achieves the goal of completely eliminating spurious correlations. To accomplish this feat without significantly altering the streamwise extent of our domain, it is clear that some additional amount of scrambling must be used. Thus, we consider the dynamic improvements RR + DS and RR + DR.

In Figs. 11a–11d, we plot the correlation maps associated with the dynamic methods RR + DS (Figs. 11a and 11b) and RR + DR (Figs. 11c and 11d). It is clear from these plots that by altering the amount of shift or reflection location, the spurious correlations can be eliminated completely. Figures 12a–12c quantitatively compare the correlations observed in Figs. 9–11. In Fig. 12a, the temporal autocorrelation function is plotted in the outer boundary layer. This profile is equivalent to the horizontal axis on the spanwise space–time correlation plots and a horizontal slice across the streamwise space–time correlation plots at $\Delta x/\delta_r = 0$. The spurious peaks at one and two FTTs (actually just after, due to the velocity in the boundary layer being somewhat less than freestream) are clearly observable; additionally, we see that the shape of the curve around $\Delta t = 0$ is unaltered for the various methods. In Fig. 12b, we plot the vertical axis of the streamwise space–time correlation plot in the inner boundary layer (where rescaling is minimal and the spurious correlation is highest). Again, we can clearly observe the spurious peak with UKRR, and we see that the streamwise integral length scale at the reference location is unaltered by any of the improved methods. Figure 12c plots the vertical axis of the spanwise space–time correlation plots and again illustrates that there is no change to the spanwise integral length scale among the methods.

To illustrate once more the effect of the nonphysical low-frequency attributes of traditional RR, we plot in Fig. 13 the temporal energy spectra of the streamwise component of the Reynolds-stress tensor. In Fig. 13a, the spectra of all methods are superimposed for comparison, and in Fig. 13b, only two are plotted for clarity. Notice that there appear to be several energetic peaks that appear in the UKRR (and sometimes RR + CS and RR + CR) signal that do not appear in the RR + DS or RR + DR signals. By including the recycling frequency, $f_{\text{rcy}}$, for comparison we see that the most intense of these peaks is located right at $f_{\text{rcy}}$ and can conclude that the additional peaks represent harmonics of the recycling frequency. By comparing the UKRR and RR+DR spectra in Fig. 13b, it is clear how much an energy spectra can be contaminated by recycling frequency harmonics. It remains to be shown, however, that the dynamic methods do not significantly alter more sensitive indicators of solution quality, a topic which will be explored in the next section.

### C. Group 3: UKRR, and Parametric Variation of RR + DR

In this section, we seek to evaluate the robustness and accuracy of dynamic improvements to the standard RR method. While we have

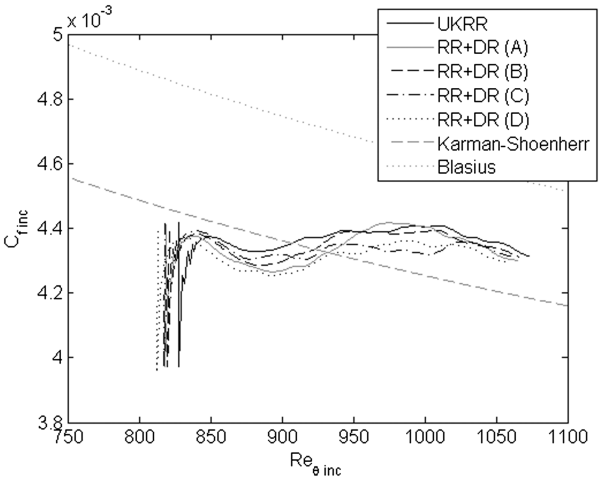


**Fig. 15 Comparison of skin friction evolution among group 3 inflow conditions.**

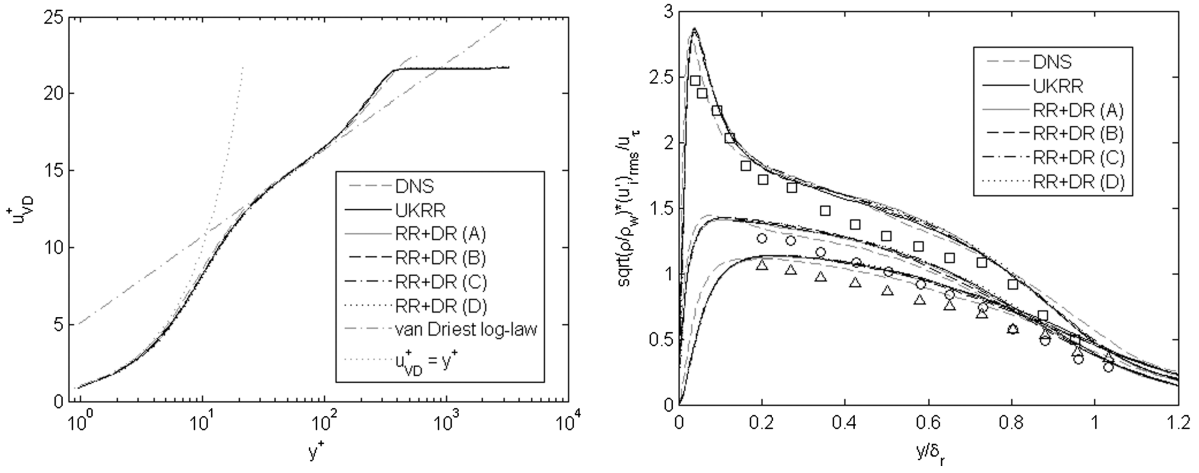


a) b)

**Fig. 14 Comparison of a) van Driest transformed mean streamwise velocity profiles and profiles (log law given by $u^+_{\text{VD}} = 5.1 + 1/0.41 * \log[y+]$) and b) density-scaled RMS turbulence intensity. Symbols taken from experiment by Erm and Jourbert [33] (□: streamwise, ○: spanwise, Δ: wall-normal).**

considered dynamic shifting and reflection separately up until this point, we will for this section consider only dynamic reflection as the work until now has provided no indication to expect that the two should perform significantly differently.

We recognize that when a reflection location "event" occurs (that is, when the reflection location is changed abruptly), this will cause discontinuities in structures at the inlet plane. Moreover, we recognize that there must exist some limit in which these events occur too frequently to provide coherent turbulence; similarly, there must exist some limit in which these events occur too infrequently to remove the spurious correlations. To explore the robustness of RR + DR, we perform a parametric variation on the streak length parameter $\lambda_{\text{rfl}}$, summarized in Table 7. Notice that RR + DR (A) is the baseline RR + DR used in Sec. IV.B. RR + DR (B) and RR + DR (C), respectively, represent simulations with more and less frequent events, and RR + DR (D) investigates a change in the mean-to-variance ratio.

Table 8 summarizes the flow properties at the reference station for each method considered in group 3. While RR + DR (D) apparently shows the most deviation in development length from the baseline UKRR, the difference is still quite small (recall that DF required a development length of $13.8\delta_r$). Figures 14 and 15 confirm this observation as well. In Figs. 14a and 14b, we again plot van Driest transformed streamwise velocity profiles and turbulence intensity profiles, respectively; and, again, we see that there is no observable difference among the group 3 methods. In Fig. 15, we plot the streamwise evolution of skin friction, and while in general it appears that the dynamic reflection methods take longer to reach equilibrium than UKRR, the difference is slight, and there does not seem to be any trend suggesting a link between $\lambda_{\text{rfl}}$ and recovery length, at least for the range under consideration.

To get a qualitative sense of what happens during a reflection location event, we show in Fig. 16 a time series of instantaneous density contours before and after an event. To illustrate how structures are broken when the event occurs, we have plotted to the left of the dashed line the appropriately reflected profile from the capture location at $y/\delta_r = 0.5$ and to the right the inlet profile at about $y/\delta_r = 0.4$ (accounting for the difference in boundary-layer thickness at the two locations). A single structure is circled immediately before and after the event occurs. As expected, the trailing end of this structure is abruptly shifted such that the resulting structure at the inlet is shorter than the structure which passed through the capture plane. After a very short time, however, there is no evidence of discontinuity, and the structure continues to evolve. By the time it has reached the reference location (that is, after a recovery distance indistinguishable from that of standard RR), such structures are statistically no different than those that were never broken by an event. As further qualitative evidence that the physical structure of turbulence is not significantly altered, we plot in Fig. 17 positive isosurfaces of the second invariant of the velocity gradient tensor near the inlet shortly after an event has occurred (at the fourth instant in the Fig. 16 time series).

We next wish to quantitatively assess the effect of dynamic reflection on potentially more sensitive indicators of solution quality. It is reasonable to expect that large-scale turbulent structures are most likely to be damaged by reflection events, as the finer structures will recover much faster on their own. Therefore, we would like to focus our investigation on indicators of solution quality most sensitive to large turbulent structures. In Fig. 18a, we plot the intermittency factor, which is defined as the probability that vorticity magnitude is within 1.0% of the peak average, computed using 1000 instantaneous samples spaced at intervals of $0.34\delta_r/u_\infty$. While there is some indication that the variation with the most frequent events, RR + DR (B), may have a slightly impacted intermittency factor, the effect is quite small. In Fig. 18b, we additionally plot RMS vorticity magnitude profiles at the reference location. Again, we see that there is virtually no difference among the dynamic reflection variations. Next, in Fig. 18c, we plot spanwise energy spectra of the streamwise Reynolds-stress signal in the outer boundary layer. We see that all methods generally lay right on top of one another, and we see some evidence of an inertial subrange conforming to the expected $-5/3$

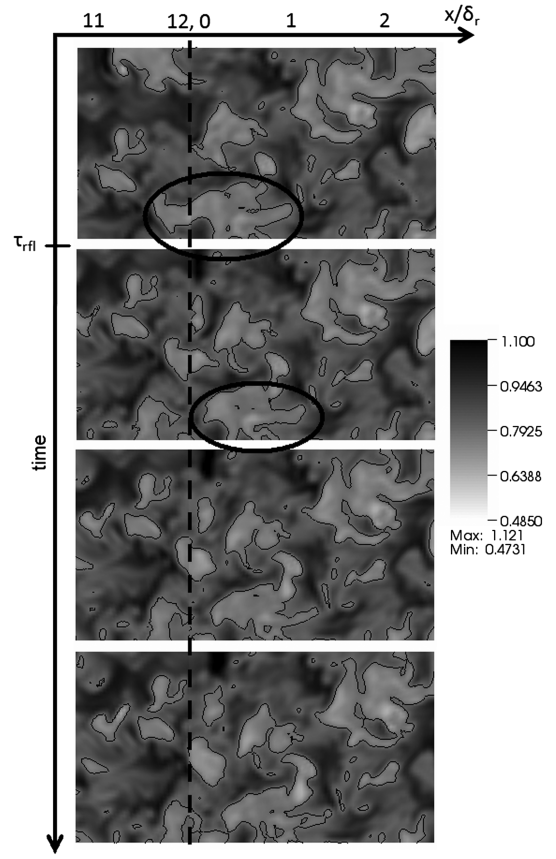


**Fig. 16 Time series of instantaneous density contours ($\rho/\rho_\infty$) at $x/\delta_r = 0$ and $y/\delta_r = 0.5$ following a reflection location event. The reflected recycling profile is plotted to the left of the inlet.**

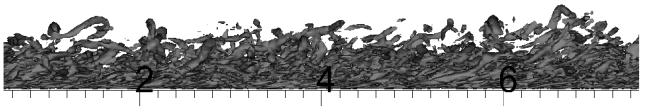


**Fig. 17 Instantaneous positive isosurfaces of the second invariant of the RR + DR (A) velocity gradient tensor ($Q = 6(\delta_r/c_\infty)^2$) near the inlet.**

scaling. The only noticeable difference seems to be in the lowest wave numbers. It appears as though the variations with the most frequent reflection location events (A, B, and D) observe somewhat less energy at $\kappa_z = 1$ than UKRR and RR + DR (C). This would seem to be consistent with the results of Fig. 13, and the cause of this discrepancy may be due to the existence of long nonphysical spanwise structures affected by the periodic boundary conditions, which are broken up more often by methods A, B, and D. Recall Fig. 12c, which demonstrates mean spanwise correlations out to about $1\delta_r$; if spanwise structures exist instantaneously with a length of $1.5\delta_r$, these structures could be perpetuated by the periodic boundary conditions and would artificially increase the energy at $\kappa_z = 1$. Since RR + DR with more frequent reflection location events would be better at breaking up these nonphysical spanwise structures, it would be expected that they should have lower energy.

It is also reasonable to assume that when reflection location events occur that there should be some spurious acoustics thrown off, and in general these could be quite significant. To assess the impact of acoustics generated, we plot in Figs. 19a and 19b RMS dilatation profiles at the inlet and at the reference location. In Fig. 19a, it is quite clear that the more frequently reflection location events occur, the greater the peak dilatation intensity is at the inlet; this, of course, confirms our suspicion that events indeed throw off spurious acoustics. However, we observe first that the maximum increase in dilatation intensity is only about 30% for the most extreme case. Additionally, we observe in Fig. 19b that at the reference location

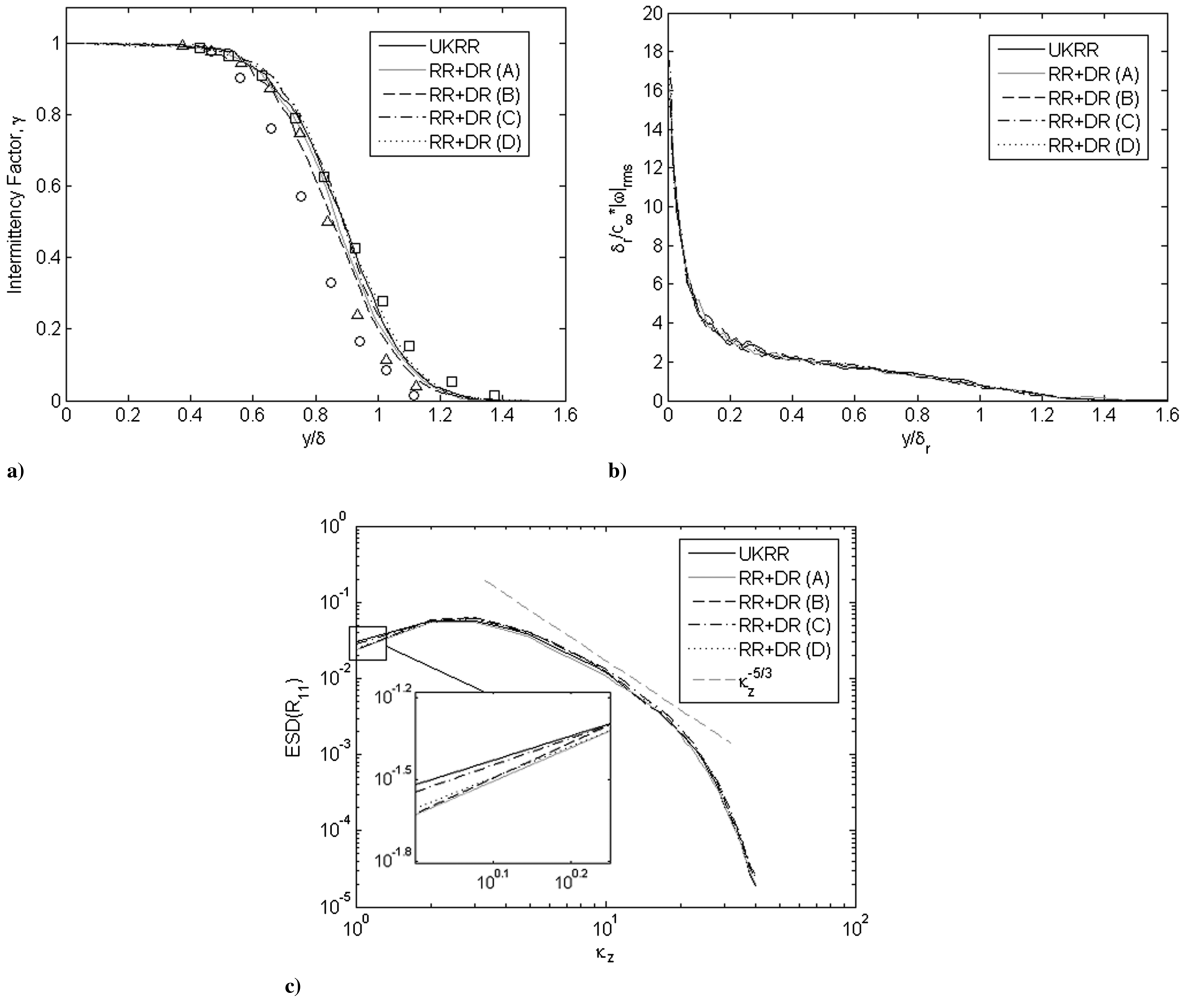


**Fig. 18 Characterization of turbulence at $x/\delta_r = x_r$: a) intermittency factor (□: Jiménez et al. [37] DNS, ○: Kovasznay et al. experiment [38], Δ: Murlis et al. experiment [39]), b) RMS vorticity magnitude, and c) energy spectral density of $R_{11}$ spanwise signal at $y/\delta_r = 0.7$.**

there appears to be no further evidence of spurious acoustics. Therefore, it seems the effect of the additional acoustics must be very minor (especially for case C).

We can observe qualitatively the effect of one such event on the dilatation field in Fig. 20. In this figure (which is meant to be read top to bottom and then left to right), a series of instantaneous dilatation fields are plotted at intervals of $0.34\delta_r/u_\infty$ following a reflection location event. The acoustic wave that is created is pointed out in each field, and its evolution can be tracked. We observe that after traveling a distance of about three to four $\delta_r$, the wave has effectively disappeared into the background pseudonoise. From this, we can conclude that the effect of any spurious acoustics created by dynamic reflection is both short-lived and not significantly stronger than the background acoustics already present.

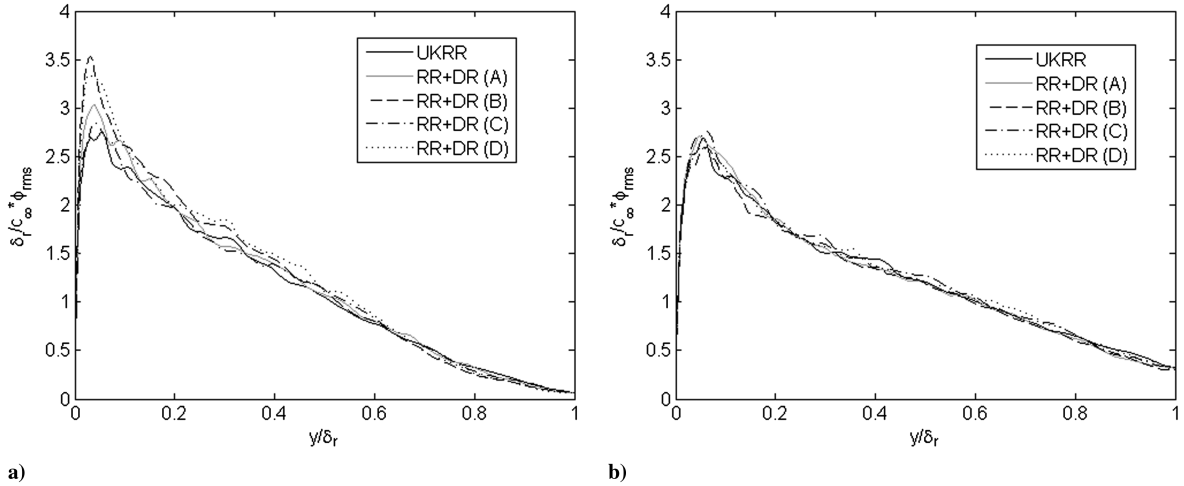


**Fig. 19 Characterization of acoustic disturbances created by discontinuous changing of reflection location: a) RMS dilatation at $x/\delta_r = 0$ and b) RMS dilatation at $x/\delta_r = x_r$.**

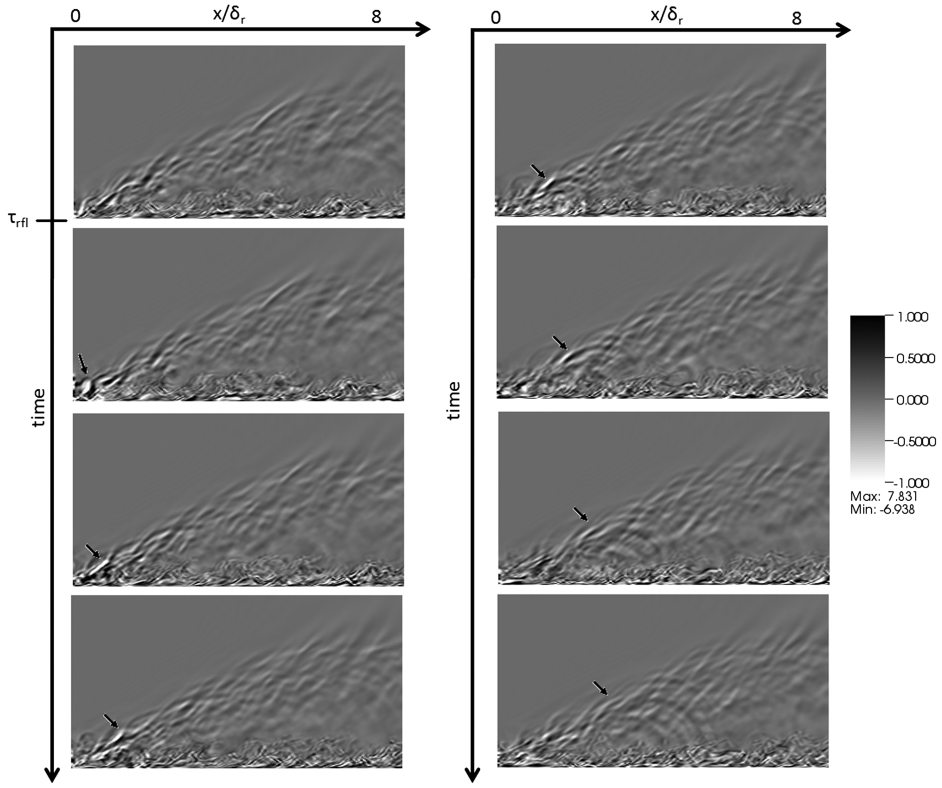


**Fig. 20 Time series of dilatation, $\delta_r/c_\infty(\nabla \cdot \mathbf{u})$, field following a reflection location event.**

**Table 9 Summary of the inflow boundary conditions considered**

| Method | Recovery length | Advantages | Disadvantages |
|---|---|---|---|
| LC | $>30\delta_r$ | Initial transient only one FTT | Requires a priori mean flow profiles |
| | | No spurious correlations | Longest recovery length |
| DF | $\sim 15\delta_r$ | Initial transient only one FTT | Requires a priori mean flow profiles |
| | | No spurious correlations | Requires a priori Reynolds-stress profiles |
| UKRR | $\sim 11\delta_r$ | Shortest recovery length | Long initial transient |
| | | Requires no a priori flow profiles | Injects nonphysical correlations |
| RR + CS | $\sim 11\delta_r$ | Shortest recovery length | Long initial transient |
| | | Requires no a priori flow profiles | Does not eliminate all spurious correlations |
| | | Changes spurious autocorrelation at one FTT to cross correlation | |
| RR + CR | $\sim 11\delta_r$ | Shortest recovery length | Long initial transient |
| | | Requires no a priori flow profiles | Does not eliminate all spurious correlations |
| | | Eliminates spurious correlation at one FTT | |
| RR + DS | $\sim 11\delta_r$ | Shortest recovery length | Long initial transient |
| | | Requires no a priori flow profiles | Introduces minimal spurious acoustics |
| | | No spurious correlations | |
| RR + DR | $\sim 11\delta_r$ | Shortest recovery length | Long initial transient |
| | | Requires no a priori flow profiles | Introduces minimal spurious acoustics |
| | | No spurious correlations | |

## V. Conclusions

In the present work, we have studied several methods to improve the standard RR procedure by means of reducing or eliminating spurious correlations related to the recycling frequency. We have compared the standard RR technique of Urbin and Knight [13] with two other commonly used synthetic methods to illuminate the potential benefits of RR if it can be improved effectively. We next demonstrated the existence of the predicted spurious correlations with standard UKRR and evaluated four potential improvements based on their ability to remove these correlations. These improvements fell into two categories of scrambling procedure (translation and reflection) and were either maintained constant or updated dynamically. Table 9 summarizes the key observations made from our comparisons.

We additionally have performed a brief parametric variation study on the parameters that control how often a reflection location is updated for the RR + DR procedure. By looking qualitatively at turbulent structures after a change in reflection location and quantitatively at mean turbulence intensities, intermittency, vorticity, and energy spectra, it was determined that the dynamic reflection procedure is quite robust with respect to the shape of the distribution from which the streak length parameter $\lambda_{\text{rfl}}$ is sampled. By looking at RMS dilatation and instantaneous dilatation fields, it was additionally confirmed that, although the dynamic reflection methods indeed throw off spurious acoustics when the reflection location is updated, the effect of these acoustics is very minimal and does not affect the dilatation profile at the reference location downstream. While this parametric variation was only performed for the dynamic reflection improvement, based on the results of Sec. IV.B, which showed no observable difference between RR + DS and RR + DR, these results are expected to be applicable to dynamic shifting as well.

Based on the work presented previously, the following conclusions can be drawn, which we feel may be used as general guidelines for the generation of inflow turbulence where low-frequency dynamics are important:

1) If no improvement is used with traditional RR, the recycling length must be quite long to naturally decorrelate: about $40\delta_r$ for the present flow conditions.

2) If a constant improvement is to be used, RR + CR is superior to RR + CS because RR + CR does not introduce a spurious cross correlation at one FTT. However, a long recycling length (about $20\delta_r$ for the present flow conditions) must still be used to naturally decorrelate the spurious correlation at two FTTs.

3) If it is advantageous to use a smaller computational domain (as is usually the case), dynamic shifting or dynamic reflection may be used with a recycling length of about $11\delta_r$ (again, this length applies only to the present flow conditions) with no significant difference in solution quality from standard RR. Furthermore, since the damage done by the discontinuous breaking of turbulent structures at the inlet apparently has negligible effect on the solution downstream, we conclude that the discontinuous dynamic methods considered are sufficient to remove unphysical temporal correlations as described.

4) The dynamic methods RR + DS and RR + DR are quite robust with respect to how often events occur; it is, therefore, recommended to use a mean streak length equal to half the recycling distance with a standard deviation of about 20% of the mean.

For flows in which low-frequency motion is important, it is desirable to ensure that inflow boundary conditions do not introduce any nonphysical correlations which might contaminate the solution. In the past, this has meant that RR procedures were rejected in favor of synthetic methods [3,4,30]. With the preceding guidelines, we hope that RR methods can now be used with confidence in flows with low-frequency motion.

## Appendix: Detailed Mathematical Models

The governing equations solved by the numerical code used in this study are the spatially filtered form of the compressible Navier–Stokes Eqs. (A1–A5):

$$\frac{\partial \rho}{\partial t} + \nabla \cdot (\rho \mathbf{u}) = 0 \tag{A1}$$

$$\frac{\partial \rho \mathbf{u}}{\partial t} + \nabla \cdot (\rho \mathbf{u}\mathbf{u} + p\bar{\delta} - \bar{\tau}) = 0 \tag{A2}$$

$$\frac{\partial E}{\partial t} + \nabla \cdot [E\mathbf{u} + (p\bar{\delta} - \bar{\tau}) \cdot \mathbf{u} - \kappa \nabla T] = 0 \tag{A3}$$

$$E = \frac{p}{\gamma - 1} + \frac{1}{2}\rho \mathbf{u} \cdot \mathbf{u}, \qquad p = \rho R T \tag{A4}$$

$$\bar{\tau} = \mu(2\bar{\mathbf{S}}) + \left(\beta - \frac{2}{3}\mu\right)(\nabla \cdot \mathbf{u})\bar{\delta}, \qquad \bar{\mathbf{S}} = \frac{1}{2}(\nabla \mathbf{u} + (\nabla \mathbf{u})^T) \tag{A5}$$

The LAD method of shock capturing is additionally used. Equations (A6–A8) describe the addition of artificial coefficients to the fluid transport terms:

$$\mu = \mu_f + \mu^* \tag{A6}$$

$$\beta = \beta_f + \beta^* \tag{A7}$$

$$\kappa = \kappa_f + \kappa^* \tag{A8}$$

Equations (A9–A12) describe the formulation of the artificial coefficients:

$$\mu^* = C_\mu \left\langle \rho \left| \sum_{l=1}^{3} \frac{\partial^r S}{\partial \xi_l^r} \Delta \xi_l^r \Delta_{l,\mu}^2 \right| \right\rangle \tag{A9}$$

$$\beta^* = C_\beta \left\langle \rho f_{\text{sw}} \left| \sum_{l=1}^{3} \frac{\partial^r \nabla \cdot \mathbf{u}}{\partial \xi_l^r} \Delta \xi_l^r \Delta_{l,\beta}^2 \right| \right\rangle \tag{A10}$$

$$\kappa^* = C_\kappa \left\langle \frac{\rho c_s}{T} \left| \sum_{l=1}^{3} \frac{\partial^r e}{\partial \xi_l^r} \Delta \xi_l^r \Delta_{l,\kappa} \right| \right\rangle \tag{A11}$$

$$f_{\text{sw}} = H(-\nabla \cdot \mathbf{u}) \times \frac{(\nabla \cdot \mathbf{u})^2}{(\nabla \cdot \mathbf{u})^2 + (\nabla \times \mathbf{u})^2 + \varepsilon} \tag{A12}$$

In Eqs. (A9–A11), $C_\mu$, $C_\beta$, and $C_\kappa$ are selected to be 0.0, 1.75, and 0.01, respectively, based on the investigation carried out in [21]. The constant $\varepsilon$ is taken to be a very small positive number (typically $1e-32$) to avoid division by zero errors in regions of zero gradient. The grid spacing is defined next in Eqs. (A13) and (A14):

$$\Delta_{l,\mu} = |\Delta x_l|, \qquad \Delta_{l,\beta} = \left| \Delta x_l \cdot \frac{\nabla \rho}{|\nabla \rho|} \right|, \qquad \Delta_{l,\kappa} = \left| \Delta x_l \cdot \frac{\nabla e}{|\nabla e|} \right| \tag{A13}$$

$$\Delta x_l = \frac{1}{2}[x_{i+1} - x_{i-1}, y_{i+1} - y_{i-1}, z_{i+1} - z_{i-1}]^T \tag{A14}$$

By defining the computational grid spacing this way, $\Delta_{l,\beta}$ is aligned perpendicular to shocks, and $\Delta_{l,\kappa}$ is aligned perpendicular to contact surfaces. The exponent $r$ is set to 4 so the artificial diffusivities are biased to high wave numbers [25]. Additionally, a van Driest wall-damping function is used to scale the physical grid spacing terms to ensure that the artificial viscosity terms vanish in the near-wall region. The code and numerical methods employed in this study are similar to those used by Kawai and Lele to investigate supersonic cross flow [26]; however, in the present study, there is no need for the computation of species diffusivity coefficients, which simplifies our formulation. Note that in the present results, since $C_\mu$ is set to zero, no artificial dynamic viscosity is being applied. Aside from the model created by addition of the artificial bulk viscosity and thermal conductivity, no additional SGS model is used. More detailed descriptions of the LAD method may be found in [21,24–26].

## Acknowledgments

This research was made with government support under and awarded by Department of Defense, Air Force Office of Scientific Research, National Defense Science and Engineering Graduate Fellowship, 32 CFR 168a. We gratefully acknowledge partial support from the Air Force Office of Scientific Research Multidisciplinary University Research Initiative, NASA Hypersonics Program, and the Department of Energy Predictive Science Academic Alliance Program. Computer time has been provided by NASA Advanced Supercomputing at NASA Ames Research Center in Moffett Field, California, and by the High Performance Computing Center at Lawrence Livermore National Laboratory in Livermore, California. We would also like to recognize M. R. Visbal at the Air Force Research Laboratory for providing the FDL3DI code that has been extended and used in the present study. Interactions with David Dawson from the Department of Aeronautics and Astronautics and Sergei Chumakov from the Center for Turbulence Research at Stanford University have also been invaluable, and the first author would like express his gratitude for the assistance.

## References

[1] Settles, G. S., Fitzpatrick, T., and Bogdonoff, S. M., "Detailed Study of Attached and Separated Compression Corner Flowfields in High Reynolds Number Supersonic Flow," *AIAA Journal*, Vol. 17, No. 6, 1979, pp. 579–585. doi:10.2514/3.61180

[2] Zheltovodov, A. A., "Advances and Problems in Modeling of Shockwave Turbulent Boundary Layer Interactions," *Proceedings of the International Conference on the Methods of Aerophysical Research*, Institute of Theoretical and Applied Mechanics,

Novosibirsk, Russia, 2004, pp. 149–157.
[3] Touber, E., and Sandham, N. D., "Oblique Shock Impinging on a Turbulent Boundary Layer: Low-Frequency Mechanisms," 38th Fluid Dynamics Conference and Exhibit, Seattle, WA, AIAA Paper 2008-4170, June 2008.
[4] Touber, E., and Sandham, N. D., "Large-Eddy Simulation of Low-Frequency Unsteadiness in a Turbulent Shock-Induced Separation Bubble," *Theoretical and Computational Fluid Dynamics*, Vol. 23, No. 2, 2009, pp. 79–107. doi:10.1007/s00162-009-0103-z
[5] Pirozzoli, S., and Grasso, F., "Direct Numerical Simulation of Impinging Shock Wave/Turbulent Boundary Layer Interaction at $M = 2.25$," *Physics of Fluids*, Vol. 18, No. 6, 2006, pp. 065113-1–065113-17. doi:10.1063/1.2216989
[6] Yao, Y. F., and Sandham, N. D., "DNS of Turbulent Flow over a Bump with Shock/Boundary-Layer Interactions," *Fifth International Symposium on Engineering Turbulence Modeling and Measurements*, Mallorca, Spain, 2002, pp. 677–686.
[7] Li, Q., and Coleman, G. N., "DNS of an Oblique Shock Wave Impinging upon a Turbulent Boundary Layer," *Direct and Large-Eddy Simulation V*, edited by R. Friedrich, B. J. Geurts, and O. Metais, Kluwer Academic, Dordrecht, The Netherlands, 2003, pp. 387–396.
[8] Klein, M., Sadiki, A., and Janicka, J., "A Digital Filter Based Generation of Inflow Data for Spatially Developing Direct Numerical or Large Eddy Simulations," *Journal of Computational Physics*, Vol. 186, No. 2, 2003, pp. 652–665. doi:10.1016/S0021-9991(03)00090-1
[9] Xie, Z. T., and Castro, I. P., "Efficient Generation of Inflow Conditions for Large-Eddy Simulations of Street-Scale Flows," *Flow, Turbulence and Combustion*, Vol. 81, No. 3, 2008, pp. 449–470. doi:10.1007/s10494-008-9151-5
[10] Jarrin, N., Benhamadouche, S., Laurence, D., and Prosser, R., "A Synthetic-Eddy-Method for Generating Inflow Conditions for Large-Eddy Simulations," *International Journal of Heat and Fluid Flow*, Vol. 27, No. 4, 2006, pp. 585–593. doi:10.1016/j.ijheatfluidflow.2006.02.006
[11] Pamiès, M., Weiss, P., Garnier, E., Deck, S., and Sagaut, P., "Generation of Synthetic Turbulent Inflow Data for Large Eddy Simulation of Spatially Evolving Wall-Bounded Flows," *Physics of Fluids*, Vol. 21, No. 4, 2009, pp. 045103-1–045103-15. doi:10.1063/1.3103881
[12] Lund, T. S., Wu, X., and Squires, K. D., "Generation of Turbulent Inflow Data for Spatially-Developing Boundary Layer Simulations," *Journal of Computational Physics*, Vol. 140, No. 2, 1998, pp. 233–258. doi:10.1006/jcph.1998.5882
[13] Urbin, G., and Knight, D., "Large-Eddy Simulation of a Supersonic Boundary Layer Using an Unstructured Grid," *AIAA Journal*, Vol. 39, No. 7, 2001, pp. 1288–1295. doi:10.2514/2.1471
[14] Xu, S., and Martin, M. P., "Assessment of Inflow Boundary Conditions for Compressible Turbulent Boundary Layers," *Physics of Fluids*, Vol. 16, No. 7, 2004, pp. 2623–2639. doi:10.1063/1.1758218
[15] Spalart, P. R., Strelets, M., and Travin, A., "Direct Numerical Simulation of Large-Eddy-Break-Up Devices in a Boundary Layer," *International Journal of Heat and Fluid Flow*, Vol. 27, No. 5, 2006, pp. 902–910. doi:10.1016/j.ijheatfluidflow.2006.03.014
[16] Boles, J. A., Choi, J., and Edwards, J. R., "Simulations of High-Speed Internal Flows Using LES/RANS Models," 47th AIAA Aerospace Sciences Meeting Including the New Horizons Forum and Aerospace Exposition, Orlando, FL, AIAA Paper 2009-1324, Jan. 2009.
[17] Lele, S. K., "Compact Finite Difference Schemes with Spectral-Like Resolution," *Journal of Computational Physics*, Vol. 103, No. 1, 1992, pp. 16–42. doi:10.1016/0021-9991(92)90324-R
[18] Obayashi, S., Fuji, K., and Gavali, S., "Navier–Stokes Simulation of Wind-Tunnel Flow Using LU-ADI Factorization Algorithm," NASA TM-100042, Feb. 1988.
[19] Iizuka, N., "Study of Mach Number Effect on the Dynamic Stability of a Blunt Re-Entry Capsule," Ph.D. Dissertation, Univ. of Tokyo, Tokyo, Feb. 2006.
[20] Gaitonde, D. V., and Visbal, M. R., "High-Order Schemes for Navier–Stokes Equations: Algorithm and Implementation into FDL3DI," Air Force Research Lab. AFRL-VA-WP-TR-1998-3060, 1998.
[21] Kawai, S., Shankar, S. K., and Lele, S. K., "Assessment of Localized Artificial Diffusivity Scheme for Large-Eddy Simulation of Compressible Turbulent Flows," *Journal of Computational Physics*, Vol. 229, No. 5, 2010, pp. 1739–1762. doi:10.1016/j.jcp.2009.11.005
[22] Cook, A. W., "Artificial Fluid Properties for Large-Eddy Simulation of Compressible Turbulent Mixing," *Physics of Fluids*, Vol. 19, No. 5, 2007, pp. 055103. doi:10.1063/1.2728937
[23] Mani, A., Larsson, J., and Moin, P., "Suitability of Artificial Bulk Viscosity for Large-Eddy Simulation of Turbulent Flows with Shocks," *Journal of Computational Physics*, Vol. 228, No. 19, 2009, pp. 7368–7374. doi:10.1016/j.jcp.2009.06.040
[24] Kawai, S., Shankar, S. K., and Lele, S. K., "LES of Compressible Turbulent Flows: Assessment of Compact Differencing with Localized Artificial Diffusivity Scheme," AIAA Paper 2009-1505, 2009.
[25] Kawai, S., and Lele, S. K., "Localized Artificial Diffusivity Scheme for Discontinuity Capturing on Curvilinear Meshes," *Journal of Computational Physics*, Vol. 227, No. 22, 2008, pp. 9498–9526. doi:10.1016/j.jcp.2008.06.034
[26] Kawai, S., and Lele, S. K., "Large-Eddy Simulation of Jet Mixing in Supersonic Crossflows," *AIAA Journal*, Vol. 48, No. 9, 2010, pp. 2063–2083. doi:10.2514/1.J050282
[27] Dupont, P., Haddad, C., and Debiève, J. F., "Space and Time Organization in a Shock-Induced Separated Boundary Layer," *Journal of Fluid Mechanics*, Vol. 559, 2006, pp. 255–277. doi:10.1017/S0022112006000267
[28] Pirozzoli, S., and Bernardini, M., "A DNS Database for Impinging Shock Wave/Turbulent Boundary Layer Interaction," Technical Note, *AIAA Journal*, 2011 (accepted for publication).
[29] Morgan, B., Kawai, S., and Lele, S. K., "Large-Eddy Simulation of an Oblique Shock Impinging on a Turbulent Boundary Layer," *40th Fluid Dynamics Conference and Exhibit*, AIAA Paper 2010-4467, June 2010.
[30] Pirozzoli, S., Bernardini, M., and Grasso, F., "Characterization of Coherent Vertical Structures in a Supersonic Turbulent Boundary Layer," *Journal of Fluid Mechanics*, Vol. 613, 2008, pp. 205–231. doi:10.1017/S0022112008003005
[31] Stolz, S., and Adams, N. A., "Large-Eddy Simulation of High-Reynolds-Number Supersonic Boundary Layers Using the Approximate Deconvolution Model and a Rescaling and Recycling Technique," *Physics of Fluids*, Vol. 31, No. 8, 2003, pp. 2398-1–2398-15. doi:10.1063/1.1588637
[32] Smits, A., and Dussauge, J.-P., *Turbulent Shear Layers in Supersonic Flow*, American Inst. of Physics, New York, 1996, Chap. 2.
[33] Erm, L. P., and Joubert, J., "Low Reynolds Number Turbulent Boundary Layers," *Journal of Fluid Mechanics*, Vol. 230, 1991, pp. 1–44. doi:10.1017/S0022112091000691
[34] van Driest, E. R., "On Turbulent Flow near a Wall," *Journal of the Aeronautical Sciences*, Vol. 23, No. 11, 1956, pp. 1007–1011, 1036.
[35] Hopkins, E. J., and Inouye, M., "An Evaluation of Theories for Predicting Turbulent Skin Friction and Heat Transfer on Flat Plates at Supersonic and Hypersonic Mach Numbers," *AIAA Journal*, Vol. 9, No. 6, 1971, pp. 993–1003. doi:10.2514/3.6323
[36] Pirozzoli, S., Grasso, F., and Gatski, T. B., "Direct Numerical Simulation and Analysis of a Spatially Evolving Supersonic Turbulent Boundary Layer at $M = 2.25$," *Physics of Fluids*, Vol. 16, No. 3, 2004, pp. 530–545. doi:10.1063/1.1637604
[37] Jiménez, J., Hoyas, S., Simens, M. P., and Mizuno, Y., "Turbulent Boundary Layers and Channels at Moderate Reynolds Numbers," *Journal of Fluid Mechanics*, Vol. 657, 2010, pp. 335–360. doi:10.1017/S0022112010001370
[38] Kovasznay, L., Kibens, V., and Blackwelder, R., "Large-Scale Motion in the Intermittent Region of a Turbulent Boundary Layer," *Journal of Fluid Mechanics*, Vol. 41, No. 02, 1970, pp. 283–325. doi:10.1017/S0022112070000629
[39] Murlis, J., Tsai, H., and Bradshaw, P., "The Structure of Turbulent Boundary Layers at Low Reynolds Numbers," *Journal of Fluid Mechanics*, Vol. 122, No. 1, 1982, pp. 13–56. doi:10.1017/S0022112082002080

P. Tucker
*Associate Editor*